International Journal of Multiphase Flow 101 (2018) 47–63

Contents lists available at ScienceDirect

International Journal of Multiphase Flow

journal homepage: www.elsevier.com/locate/ijmulflow

Dynamics of liquid–liquid flows in horizontal pipes using simultaneous two–line planar laser–induced fluorescence and particle velocimetry

Roberto Ibarra, Ivan Zadrazil, Omar K. Matar, Christos N. Markides*

Department of Chemical Engineering, Imperial College London, South Kensington Campus, London SW7 2AZ, UK

ARTICLE INFO

Article history:
Received 30 April 2017
Revised 21 December 2017
Accepted 22 December 2017
Available online 23 December 2017

Keywords:
Oil–water pipe flow
Planar laser–induced fluorescence
Particle velocimetry
Velocity profiles
Velocity fluctuations
Turbulence characteristics
Mixing length

ABSTRACT

Experimental investigations are reported of stratified and stratified–wavy oil–water flows in horizontal pipes, based on the development and application of a novel simultaneous two–line (two–colour) technique combining planar laser–induced fluorescence with particle image/tracking velocimetry. This approach allows the study of fluid combinations with properties similar to those encountered in industrial field–applications in terms of density, viscosity, and interfacial tension, even though their refractive indices are not matched, and represents the first attempt to obtain detailed, spatiotemporally–resolved, full 2–D planar–field phase and velocity information in such flows. The flow conditions studied span mixture velocities in the range 0.3–0.6 m/s and low water–cuts up to 20%, corresponding to in situ (local) Reynolds numbers of 1750–3350 in the oil phase and 2860–11,650 in the water phase, and covering the laminar/transitional and transitional/turbulent flow regimes for the oil and water phases, respectively. Detailed, spatiotemporally–resolved in situ phase and velocity data in a vertical plane aligned with the pipe centreline and extending across the entire height of the channel through both phases are analysed to provide statistical information on the interface heights, mean axial and radial (vertical) velocity components, (rms) velocity fluctuations, Reynolds stresses, and mixing lengths. The mean liquid–liquid interface height is mainly determined by the flow water cut and is relatively insensitive (up to 20% the highest water cut) to changes in the mixture velocity, although as the mixture velocity increases the interfacial profile transitions gradually from being relatively flat to containing higher amplitude waves. The mean velocity profiles show characteristics of both laminar and turbulent flow, and interesting interactions between the two co–flowing phases. In general, mean axial velocity profiles in the water phase collapse to some extent for a given water cut when normalised by the mixture velocity; conversely, profiles in the oil phase do not. Strong vertical velocity components can modify the shape of the axial velocity profiles. The axial turbulence intensity in the bulk of the water layer amounts to about 10% of the peak mean axial velocity in the studied flow conditions. In the oil phase, the axial turbulence intensity increases from low values to about 10% at the higher Reynolds numbers, perhaps due to transition from laminar to turbulent flow. The turbulence intensity showed peaks in regions of high shear, i.e., close to the pipe wall, and at the liquid–liquid interface. The development of the mixing length in the water phase, and also above the liquid–liquid interface in the oil phase, agrees reasonably well with predicted variations described by the von Karman constant. Finally, evidence of secondary flow structures both above and below the interface exists in the vertical velocity profiles, which is of interest to explore further.

1. Introduction

The internal flow of two immiscible liquids in channels is commonly encountered in a wide variety of industrial applications across scales, from microfluidic mixers to export pipelines in subsea oil production systems. Yet, even the behaviour of model systems of co–current two–phase (liquid–liquid) flows of simple fluids in horizontal pipes remains not fully understood due to the complex interactions between the two liquid phases in which interfacial forces, wetting characteristics, phenomena such as phase inversion and, at higher Reynolds numbers, turbulence, result in a wide range of possible flow regimes. These regimes, which are strongly dependent on the fluid properties (density, viscosity, and

* Corresponding author.
E-mail addresses: r.ibarra-hernandez13@imperial.ac.uk (R. Ibarra), i.zadrazil06@imperial.ac.uk (I. Zadrazil), o.matar@imperial.ac.uk (O.K. Matar), c.markides@imperial.ac.uk (C.N. Markides).

https://doi.org/10.1016/j.ijmultiphaseflow.2017.12.018

interfacial tension), flow velocities, and pipe characteristics (diameter, inclination, roughness, and wettability), can be classified into two main categories: separated and mixed flows. Separated flows are associated generally with the existence of two continuous fluid layers on either side of a continuous interface that can be smooth or wavy, while mixed flows are more complex due to the appearance of droplets of one phase in the other (e.g., dual continuous, water–in–oil dispersions).

Horizontal liquid–liquid flows have been studied by a number of researchers, for example, Russell et al., (1959); Charles et al., (1961); Arirachakaran et al., (1989); Trallero (1995); Soleimani (1999); Angeli and Hewitt (2000); and references therein. The main purpose of these pioneering studies was to characterise these flow in terms of flow–regime maps, pressure gradients and in situ phase fractions, which they achieved by employing a number of intrusive and/or spatially–integrative and low–spatial–resolution measurement techniques such as quick–closing valves, pressure transducers, impedance probes, conductivity probes, and mesh sensors.

Further (e.g., velocity) information can be provided by hot–film probes, which make it possible to measure with excellent temporal resolution the time–varying velocity (mean and fluctuating components thereof) in liquid–liquid flows. However, the intrusive nature of this measurement can affect the flow in the region around the probe, thereby modifying the flow such that it may not represent the conditions of the system under study, especially in flows with significant turbulence levels, and does not allow reliable measurements at or near the interface.

The aforementioned techniques are not able to supply detailed, space– and time–resolved, full flow–field information, which is essential in promoting our understanding of these systems and for the development of reliable predictive models. This has led to the development of non–intrusive measurement techniques, based on the use of laser systems. The first laser–based technique used in the extraction of local, in situ flow velocities was Laser Doppler Anemometry (LDA), employed by Yeh and Cummins (1964) to obtain velocity profiles in single–phase water flows. While this technique offers high spatial resolution and fast dynamic response, and has therefore proven to be an invaluable tool for the experimental study of a wide range of flows, spatially–resolved information (i.e., instantaneous velocity fields) cannot be obtained since it is a point measurement generally limited to statistically–stationary or periodic flows if complete velocity profiles over the wall–normal coordinate are required (Morrison et al., 1994), and even then, a significant amount of time is required to interrogate an entire flow field.

Two–dimensional (2–D) spatiotemporal flow information can be obtained through the implementation of Planar–Laser Induced Fluorescence (PLIF) and/or two– or three–dimensional Particle Image or Tracking Velocimetry (PTV/PIV), which can also be applied simultaneously. PLIF provides information on the scalar distribution of the two phases in the plane of the laser light, while PIV/PTV can provide instantaneous velocity fields which are essential for obtaining profiles of mean velocity, turbulence intensity, Reynolds stresses, as well as the strain rates at near–wall/near–interface regions. PLIF has been employed to characterise falling–film flows over flat plates (Charogiannis et al., 2015; Markides et al., 2016), gas–liquid annular vertical flows (Schubring et al., 2010; Zadrazil et al., 2014), co–current liquid–liquid vertical downward pipe flows (Liu, 2005), and co–current liquid–liquid flows in horizontal pipes (Morgan et al., 2012; 2013; 2017). In PLIF, a horizontal flow is typically illuminated by a thin laser light sheet passing through a vertical plane aligned with the pipe centreline. A distinction between the phases is achieved by the addition of a fluorescent dye in one of the phases. The fluorescent dye is excited by the laser light and emits spectrum–shifted light that is then captured by a high–speed camera.

In 2–D PIV/PTV, a laser light sheet is used to illuminate the flow (as in PLIF) and the Mie–scattered light from seeded particles in the flow is captured by a high–speed camera. The positions of the particles in instantaneous, successive image–pairs are cross–correlated to obtain displacement and, thus, velocity data. In PIV, the cross–correlation is performed on particle groups within defined windows, while in PTV it is performed on individual particles typically following PIV processing passes. PIV and PTV have been used to obtain velocity information in gas–liquid systems, e.g., by Zadrazil and Markides (2014) and also Ashwood et al., (2015) who obtained velocity information inside the liquid film in downward gas–liquid annular flow with different approaches, while Ayati et al., (2014) performed simultaneous PIV measurements in horizontal stratified air–water pipe flows, and Birvalski et al., (2014) obtained measurements of velocity and wave characteristics in the liquid layer of gas–liquid stratified flows in circular horizontal pipes, in all cases supplying invaluable information on the flows of interest.

The aforementioned optical techniques are associated with their own set of challenges. In liquid–liquid systems, attempts have been made to match the refractive indices (RIs) of the test fluids for the purpose of minimising light refraction or reflection at the interface. However, this often results in the selection of fluids with physical properties significantly different to those encountered in common field–applications, potentially leading to flows not entirely representative of actual industrial applications. In an excellent effort, Conan et al., (2007) performed experiments in dispersed–stratified flows in a 50–mm internal diameter horizontal acrylic pipe using RI–matched fluids (i.e., heptane and a 50% vol. aqueous–glycerol solution) to obtain detailed velocity and shear information near the wall and at the interface with PIV. Similarly, Morgan et al., (2013) performed PLIF and PIV experiments in liquid–liquid flows in a 25.4–mm internal diameter horizontal stainless–steel pipe (with a borosilicate glass measuring section) using the RI–matched pair of Exxsol D80 and an 81.7% wt. aqueous–glycerol solution, which also matched the RI of the borosilicate measuring section, thus further minimising optical distortions. Simultaneous information in both phases was obtained using a single laser–sheet; however, the viscosity of the resulting glycerol solution was approximately 43 times higher than that of the oil phase, which is not commonly observed in industrial applications with the exception of oil–water systems with ethylene glycol used to prevent the formation of hydrates.

In another particularly interesting effort, Kumara et al., (2010) employed PIV to characterise the flow structures in oil–water flow in a 56–mm diameter stainless steel pipe. The RIs of the test fluids were not matched, hence, the light was refracted as it passed through the liquid–liquid interface enabling accurate information to be obtained in only one phase (i.e., before the light reached the interface). The experimental procedure was carried out in two steps: firstly, the flow was illuminated with the laser sheet from top to bottom to obtain information in the (top) oil phase; secondly, the laser sheet was introduced from the bottom of the pipe to obtain information in the water phase. This proved to be a very worthy effort in terms of supplying statistical information in the two liquid phases, but even so, in some cases, it is of interest to generate simultaneous information in both phases.

The need for this type of information motivated the development of a simultaneous planar combined LIF and PIV/PTV technique in the present work, which employs a second laser–sheet at a different wavelength, and its application to the horizontal liquid–liquid flows of interest that feature two test fluids with different RIs. To the best of the authors' knowledge, the present work represents the first attempt to obtain detailed, spatiotemporally–resolved, full planar–field phase and 2–D velocity information in such flows of selected fluids with mismatched RIs.

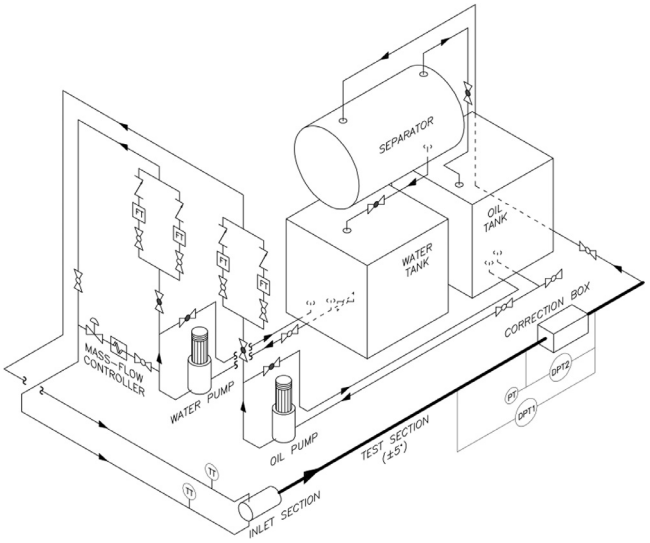

Fig. 1. Schematic of the TOWER flow facility (FT: turbine flowmeter, TT: temperature transducer, DPT differential pressure transducer, PT: pressure transducer).

The available literature on the detailed, spatiotemporally–resolved measurement of liquid–liquid pipes flows is limited, with most previous studies employing RI–matched fluids that do not represent certain industrial field–applications of interest to this research. This work aims to improve our understanding and provide new experimental data on horizontal liquid–liquid flows over a range of conditions of interest, and specifically on the interface levels, mean flow velocities and flow unsteadiness, by the implementation of the aforementioned technique. It is noted that the present study is focused on planar, 2–D velocity vector maps in the plane of illumination, nevertheless, the techniques can be extended to obtain velocity information on the third (out–of–plane) component (see Elsinga and Ganapathisubramani, 2013), e.g., holographic–particle image velocimetry (H–PIV), scanning–PIV, 3–D particle tracking, amongst other. For an excellent review of the use of PIV and H–PIV for the quantification of 3–D flow structures the reader is referred to Katz and Sheng (2010) and Westerweel et al., (2013), respectively.

The rest of this paper is organised as follows. The flow facility used in this study is described in Section 2, along with the laser–based diagnostic technique and image–processing steps. The experimental results and analysis of the observed flow characteristics are presented and discussed in Section 3. Finally, Section 4 contains the main conclusions of the study.

2. Experimental methods

2.1. Flow facility, apparatus and test fluids

The experimental investigations on which the present paper is based were performed in a multiphase flow facility known as TOWER (Two–phase Oil–Water Experimental Rig) located at Imperial College London, which is illustrated in Fig. 1.

The experimental facility allows investigation of co–current flows of two immiscible phases in horizontal or slightly inclined pipes. Water and an aliphatic oil (Exxsol D140) were used as the test liquids in the present study. Their physical properties, which are shown in Table 1, fall within the range of properties encountered in an actual industrial field–application of interest to this research.

The closed flow–loop of TOWER consists of two storage tanks (one for each of liquid phase; oil and water) with a maximum capacity of 680 L each, each one of which is connected to a vertical pump with a nominal capacity of 160 L/min that delivers the liquids (separately) to the test section. The volumetric flow rates of each liquid phase were measured with a combination of two turbine flowmeters, which have a capacity of 2–20 L/min and 14–140 L/min, and an accuracy of ± 0.5% of full scale. Low water flow rates were measured using a Coriolis mass–flow controller, which has a range of 5–300 kg/hr (0.08–5 L/min based on the water density) and an accuracy of ± 0.2% of the measured value. Flowmeters with different measuring ranges were employed to reduce the flow–rate measurement uncertainty over the full range of investigated flow conditions.

Table 1
Physical properties of the test liquids.

	Oil Exxsol D140	Water
Density, ρ (kg/m^3)	824	998
Interfacial tension, γ (mN/m)	35.1	
Refractive index, RI	1.456	1.333
Viscosity, μ at 25 °C (mPa·s)	5.4	0.9

The two liquids were introduced into the test pipe through a specially–designed inlet section featuring a horizontal splitter–plate; the inlet section design is described in Section 2.2. The main pipe test section has an internal diameter of $D = 32$ mm and a total length of 8.5 m, and consists of 5 acrylic and fused quartz–glass pipe sections connected with acrylic flanges. The scaling of observations and findings from studies such as the present to larger pipes, based on a non–dimensional analysis approach has been considered in Ibarra et al., (2014, 2015). The first three sections are made of acrylic pipe with lengths of 1, 2 and 2 m, while the fourth and final sections comprise a 2–m long quartz pipe and a 1.5–m long acrylic pipe, respectively. The average uncertainty in the elevation difference at the horizontal configuration was estimated at ± 2.1 mm over the total pipe length. For the purpose of reducing optical distortions, the optical measurement location was located in the quartz pipe section, $L/D = 209$ from the inlet, since quartz matches the RI of the oil phase (Wright et al., 2017).

Optical measurement sections often comprise a short transparent pipe providing visual access and made of a different material than the rest of the test section, which is typically metallic (e.g., stainless steel as in Morgan et al., 2013). Differences in wettability (measured by the contact angle) between the liquids and the pipe wall can locally affect the flow as it passes through these sections. In our case, the oil–water–acrylic and oil–water–quartz contact angles α on an oil pre–wetted substrate are $\alpha = 108.7 \pm 2.9°$ and $\alpha = 59.2 \pm 2.3°$, respectively. For this reason, a long quartz pipe is selected as the measurement section in our work, and the optical measurements are performed at the farthest point from acrylic/quartz transition at $L/D = 53$ from this point. By visual observation, minor changes to the oil–water contact line at the pipe wall as this flowed from the acrylic pipe section into the quartz measurement section were found to decay by a length of about 15–20 D from the transition.

The development of the flow was examined with readings from two differential pressure transducers installed along the test section, from which data was recorded simultaneously with the laser–based measurements. These transducers (DPT1 and DPT2, as shown in Fig. 1) measured pressure drops over distances of $L/D = 136$ and 66 with an entry length of $L/D = 92$ and 155, respectively. The difference in the mean measured values from the two pressure transducers was less than ± 5% in our measurements, which would be expected if the flow was fully developed at the measurement section (i.e., $L/D = 209$).

After the test liquids pass through the test section, they are collected, separated in a horizontal liquid–liquid separator equipped with a coalescing mesh, and flow under the action of gravity into

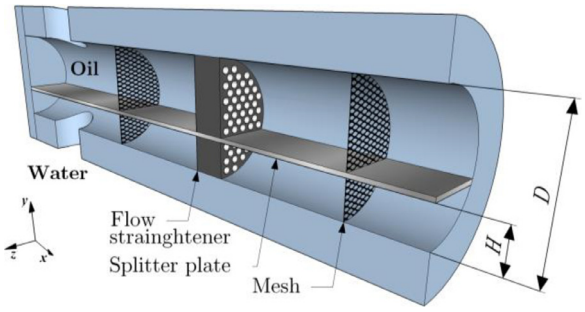

Fig. 2. TOWER inlet section design, where D and H denote the internal diameter and the clearance height of the splitter plate above the bottom of the pipe; here $H/D = 0.31$.

separate storage tanks, from where they are pumped again into the test pipe.

2.2. Inlet section design

The TOWER inlet section comprises a circular channel with a series of flow conditioners (grids, honeycomb cores) and a splitter plate, as shown in Fig. 2. The splitter plate, whose purpose is to promote initially–stratified flows and prevent the liquids from mixing inside the inlet section, was positioned at a height of $H = 10$ mm from the bottom of the channel. The flow conditioning aims to obstruct large–scale flow structures such as secondary flows at the inlet, and to make the velocity profile more uniform before both phases flow into the test section. The water and oil phases were introduced into the inlet from the bottom and top of the section, respectively.

2.3. Flow conditions and experimental procedure

Experimental data were acquired for various inlet water cuts and mixture velocities. The water cut is defined as the ratio between the water and total volumetric flow rates as introduced to the inlet section and measured by the flow meters, $WC = Q_W/Q_T$ where $Q_T = Q_W + Q_O$, and the (bulk) mixture velocity as the area–averaged total volumetric flow rate, $U_m = Q_T/A$ with A being the cross–sectional area of the pipe, $A = \pi D^2/4$. The inlet water cut, WC, was varied between 5 and 20% and the mixture velocity, U_m, between 0.2 and 0.6 m/s.

The water cut and the mixture velocity were kept constant during each experimental run (steady–state conditions). All runs were performed at near atmospheric pressure and at a temperature of 25 ± 2 °C. The pressure drop was recorded using pressure transducers with an accuracy of $\pm 0.15\%$ of full span (i.e., 3 kPa), and the temperatures of both fluids were measured with K–type thermocouples located upstream of the inlet section. A LabVIEW® control panel was built to operate and control the flow system, and to acquire the experimental conditions.

Based on the above conditions, an in situ (at the optical measurement location) Reynolds number can be defined for phase i as $Re_i = \rho_i U_i D_{hi}/\mu_i$. This definition is based on the bulk in situ fluid velocity $U_i = Q_i/A_i$ where A_i is the cross–sectional area occupied by the respective liquid, and the hydraulic diameter D_{hi} of each fluid calculated from the liquid/pipe wetted perimeters, S_i, based on the mean water layer height, $\langle h_w \rangle$ from the expression $D_{hi} = 4A_i/S_i$. The full set of investigated flow conditions covered in the present experiment campaign is given in Table 2.

2.4. Optical diagnostic techniques

Any optical diagnostic technique employed for the study of two–phase flows in pipes must take into account the refraction or reflection of light as it passes through all fluid–pipe (i.e., both on the inside and outside of the pipe) and fluid–fluid interfaces. Ideally, a fully RI–matched system is desired to avoid such optical distortions (Wright et al., 2017). However, this is a challenging task to accomplish for liquids and pipe materials with properties comparable to those encountered in actual practical applications. In the present study, the test pipe had a similar RI (i.e., 1.456) to the oil phase, resulting in minimal optical distortions at the oil–pipe wall interface.

Table 2
Inlet mixture velocities, water cuts and corresponding in situ Reynolds numbers (see text for all definitions) for the experimental condition envelope investigated in this work.

U_m (m/s)	WC (%)	Re_{oil}	Re_w
0.3	20	1850	5820
	10	1810	4140
	5	1750	2860
0.4	20	2410	7790
	10	2400	5450
	5	2390	3950
0.5	20	3080	9600
	10	2860	6510
0.6	20	3350	11,650

Inevitable optical distortions remained at the other (water–pipe wall) fluid interface due to the difference in the RI there, and these were intensified by the circular shape (curvature) of the pipe, especially close to the pipe wall. These distortions were reduced by placing a rectangular correction box around the test pipe at the measurement location, made of acrylic and filled with oil, after which they were corrected for by using a graticule target as described in Section 2.5.

The PLIF–PIV/PTV optical measurement apparatus employed a Cu–vapour laser, which emits two narrow–band laser beams at 510.6 nm (green) and 578.2 nm (yellow) with a nominal (total) output power of 20 W at a frequency of 10 kHz, a pulse–duration of 2 ns and a pulse energy of 2 mJ. Each beam was delivered to a separate sheet generator by a fibre–optic cable. The 510.6 nm and 578.2 nm sheet generators were located above and below the correction box, respectively, as shown in Fig. 3. The thickness of the laser sheets was approximately 1 mm at the measurement plane, and the width was expanded using plano–concave cylindrical lenses to illuminate the combined field–of–view of the cameras that covered the entire height of the flow.

Two cameras were used to record simultaneously the two liquid phases, as shown in Fig. 3b: (1) an Olympus iSpeed 3 with a maximum resolution of 1280×1024 pixels at a maximum frame–rate of 2 kHz (bottom camera) equipped with a Nikkor 60–mm lens, and (2) an Olympus iSpeed 2, inclined at 20° to the horizontal, with a maximum resolution of 800×600 pixels at a maximum frame–rate of 1 kHz (top camera) equipped with a Nikkor 50–mm lens.

A fluorescent dye was added to the water phase in order to obtain a clear distinction between the phases and, therefore, to identify clearly the liquid–liquid interface. The excitation and emission spectra of the fluorescent dye are of importance for the selection of a suitable dye for the PLIF measurement. It was found that the dye Eosin Y, which is soluble in water, has an excitation peak at 524 nm, a normalised excitation of 54% at 510.6 nm (green light), and no excitation at 578.2 nm (yellow light). This allowed excitation by (only) one of two the laser wavelengths, and a distinction of the resulting fluorescence from the Mie scattered light.

The flow velocity was determined by cross–correlating seeded–particle positions in consecutive images. These particles must be small enough to follow the flow and yet be able to scatter enough light to be captured by the high–speed cameras. Kumara et al., (2010) employed polyamide particles with a mean particle diameter of 20 µm and a density of 1.03 g/cm^3. Pouplin et al., (2015) used

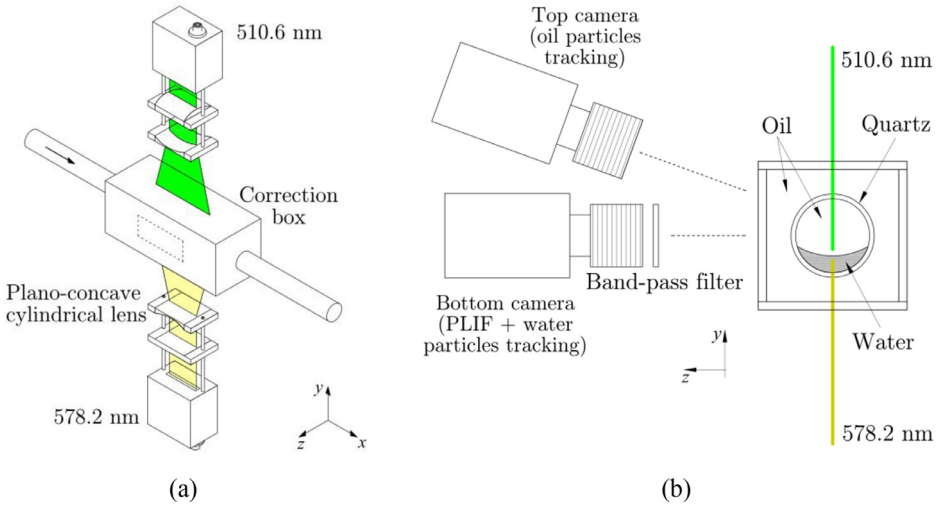

Fig. 3. Optical diagnostic technique schematics: (a) laser sheet arrangement at the measurement section, and (b) high–speed camera arrangement. (For interpretation of the references to colour in this figure, the reader is referred to the web version of this article.)

fluorescent PMMA particles encapsulated with Rhodamine B with a particle diameter range between 1 and 20 µm and a density of 1.18 g/cm^3 for the study of a flow of heptane and 43% wt. aqueous–glycerol solution in a horizontal pipe. Kolaas et al., (2015) utilised 70 µm polyamide particles for the study of liquid–solid flow in a 50–mm ID horizontal pipe. In this work, hollow glass–spheres (LaVision 110P8) with a mean diameter of 10 µm and a density of 1.1 g/cm^3, and silver coated glass spheres (HART AGSF–20) with a mean diameter of 50 µm and a density of 0.8 g/cm^3, were seeded into the water and oil phases, respectively. The Stokes number of the seeded particles, defined here as $Stk = \rho_p d_p{}^2 U_c/(18\mu_c D)$ where ρ_p is the density of the particles, d_p is the diameter of the particles, U_c and μ_c are the velocity and viscosity of the continuous phase, respectively, can be used to determine if the particles response time is fast enough to follow the fluid velocity and direction. The Stokes numbers based on a fluid velocity twice the maximum mixture velocity studied are less than 10^{-3} for both the oil and water phases, so the particles can be assumed to follow the flow reliably in the current flow system.

The yellow laser sheet was used to illuminate the particles in the water phase, and the green light to illuminate the particles in the oil phase and to excite the fluorescent dye added to the water phase. The bottom high–speed camera captured the scattered light from the particles in the water phase (at 578.2 nm) and the re–emitted light from the fluorescent dye while blocking the green light at 510.6 nm with the use of a suitable band–pass filter. This was required to avoid uncertainties in the water phase, since the RIs of both liquids are not matched. The selection of the filter requires a balance between the light intensity from the scatter particles and the re–emitted light from the fluorescent dye which is also a function of the dye concentration. A high brightness level of the re–emitted light from the fluorescence dye saturates the image preventing the detection of the scattered light from the particles while a low brightness level reduces the detection of the liquid–liquid interface. It was found that a concentration of 0.075 mL of a 5% wt. solution of Eosin Y (Sigma–Aldrich) per L of water and a band–pass filter centred at 580 nm with a width of ± 10 nm (Edmund Optics, part no. 65–222) resulted in optimum light brightness levels. The effect of the fluorescent dye on the fluid properties (i.e., density, viscosity and interfacial tension) was found to be negligible at the employed concentration. The top high–speed camera captured the scatter light from the particles in the oil phase and the fluorescent dye emission, which was later removed by the masking procedure described in Section 2.5.

Images were recorded continuously over 3 s at a sampling frequency of either 500 Hz or 1 kHz, with up to two 3–s recordings made per condition, depending on the flow case. The difference in the RIs between the test fluids makes this technique applicable to flows with a single continuous interface (i.e., stratified–smooth, or wavy), in the absence of droplets of one phase in the bulk of the other. The presence of such droplets acts to distort the incident laser light, as well as the scattered and fluorescence signals, gradually reducing the accuracy of the obtained information as the complexity of the mixing increases.

2.5. Image processing

The raw instantaneous images from both cameras were first corrected for optical distortions. The correction for the (different) distortion in each set of camera images, and therefore in each phase, was performed separately by filling the pipe with one of the two test fluids without flow, and recording calibration images of a graticule target consisting of crosses with known dimension and separation inserted into the test pipe in the same plane as the laser sheet. The optical distortion corrections were later performed in the DaVis 8.3 software package (LaVision GmgH) based on these *a priori* recorded calibration images and standard algorithms in DaVis.

After correcting all raw images from both cameras for distortions, the instantaneous interface profile in each image was identified in the PLIF (bottom) camera, leading to the final result for the local and instantaneous phase distribution in each flow of interest. The corresponding spatial pixel resolution in the final PLIF processed images is 56 µm.

The interface was then used in a masking procedure where information above and below the interface was removed from the water and oil images, respectively, thus separating the images into water–only (bottom) and oil–only (top) pairs. This was done by a MATLAB code developed in–house, based on intensity levels associated with the fluorescence in the water phase. The basic steps of this processing algorithm are described below:

(1) The PLIF images (from the bottom camera) were converted into black–white binary images based on an intensity threshold value. This threshold was pre–set based on a manual calibration determined from the highest intensity levels in the water phase.
(2) Differences in the RIs between the two liquids create high–intensity reflection regions above the liquid–liquid interface,

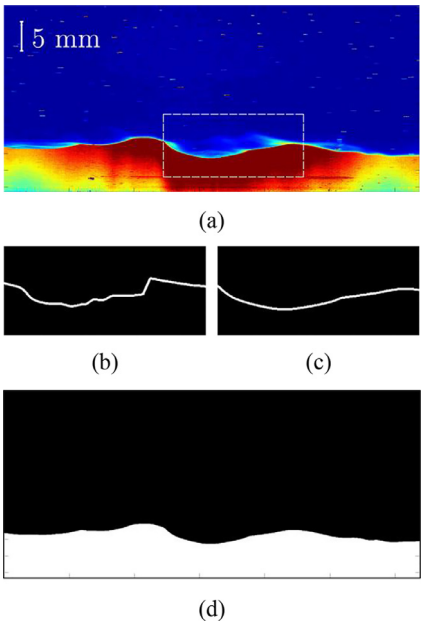

Fig. 4. PLIF image processing: (a) raw bottom camera instantaneous image, (b) interface detection in a high–reflection region (dashed region in (a)) with no correction, (c) final interface profile with reflection correction, and (d) binary image after correction based on local intensity threshold.

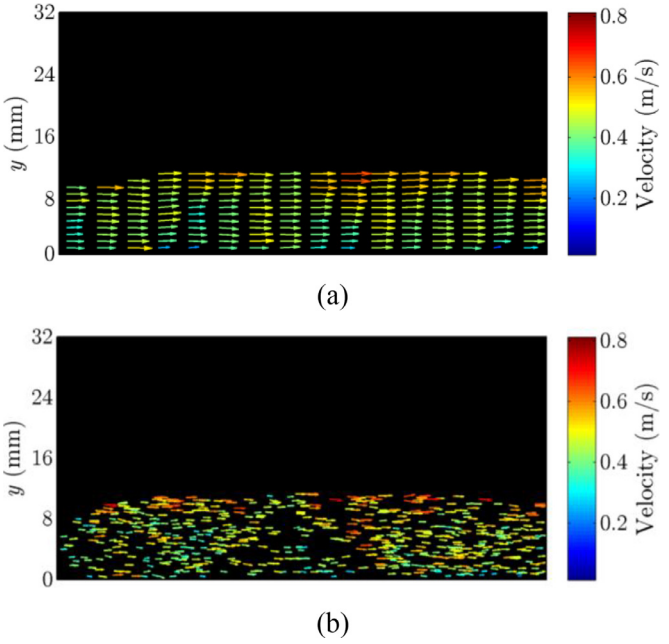

Fig. 5. Example of the water phase velocity vector field obtained from: (a) PIV, and (b) PTV, for conditions: $U_m = 0.3$ m/s, $WC = 20\%$, and a 1–kHz image acquisition frequency.

especially in wavy flows as shown in Fig. 4. This can lead to errors in detecting the liquid–liquid interface as intensity values in these regions can be higher than the pre–set intensity threshold (see Fig. 4b). This was avoided by using a moving local intensity threshold near the liquid–liquid interface region, thus enabling an accurate detection of the interface.

(3) The final instantaneous interface profiles in the bottom camera images were scaled in the x–y plane to mask the top camera images that correspond to the oil phase. This scaling was based on the relative position of the field–of–view of both images (bottom and top cameras) determined from the graticule target calibration images.

The final masked images were processed to obtain velocity information using standard PIV and PTV algorithms in DaVis, again independently for each phase (camera) using a multi–pass approach. An initial 64×64 pixel interrogation window with 50% overlap was used for the first two passes, while third and final passes were performed with a 32×32 pixel interrogation window and 50% overlap. The window sizes were selected to ensure that sufficient particles were used to determine velocity vectors. The intermediate and final PIV passes were post–processed to delete vectors based on a cross–correlation peak intensity filter and groups with less than 5 vectors. An allowable vector range was also implemented in the final PIV pass to remove vectors with velocities lower and higher than pre–defined thresholds in the axial and vertical direction. The final PIV displacement–vector resolution is 0.88 mm in the water phase and 1.27 mm in the oil phase. Finally, a PTV step was performed to resolve the large velocity gradients (e.g., close to the wall). The final PIV vector map was used as an initial estimate for the PTV vector field in which an 8×8 window was selected to track individual particles. The PTV displacement resolution is 56 µm and 82 µm in the water and oil phases, respectively. An example of the PIV and PTV velocity vector fields in the water phase is shown in Fig. 5.

The instantaneous PIV and PTV velocity vector maps were time–averaged over the total set of recordings (images) for each flow condition. Spurious vectors in the time–averaged PTV vector map, i.e., vectors that deviated significantly from the direction and magnitude of their surrounding vectors, were removed by an allowable vector range threshold based on neighbouring grids. Time–averaged vector maps were then spatially–averaged in the axial direction to provide profiles of mean velocity and characteristics related to the velocity fluctuations. The time–mean PTV vector maps were post–processed by applying a moving average function in MATLAB ("rloess"), which is based on locally–weighted polynomial regression that assigns lower weight to outliers, and used to construct mean velocity profiles in order to capture large gradients near the wall and the interface. The PIV vector maps were employed for the construction of velocity–fluctuation (e.g., Reynolds stress) profiles and were post–processed by: (1) imposing a zero value at the wall, and (2) using a shape–preserving piecewise cubic interpolation to connect values between those obtained from the PIV grid, while keeping the original values unchanged.

The time–mean local axial and radial (vertical) velocity components are defined as:

$$\langle u \rangle = \frac{1}{n} \sum_{i=1}^{n} u_i, \tag{1}$$

$$\langle v \rangle = \frac{1}{n} \sum_{i=1}^{n} v_i, \tag{2}$$

where n is the number of instantaneous velocity data points (images) used in the averaging, and u_i and v_i are the instantaneous and local axial and vertical velocity components, respectively.

Similarly, the standard deviation of the local velocity components, or velocity fluctuation rms (root–mean–square), and Reynolds stress $\langle u'v' \rangle$ are given by:

$$u_{\mathrm{rms}} = \sqrt{\frac{1}{n-1} \sum_{i=1}^{n} (u_i - \langle u \rangle)^2}, \tag{3}$$

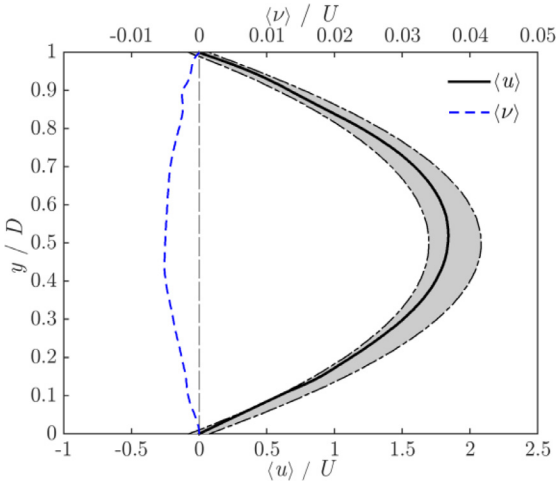

Fig. 6. Experimentally–derived single–phase (oil) mean axial, $\langle u \rangle$, and vertical, $\langle v \rangle$, velocity profiles at $Re = 1800$, normalised by the bulk flow velocity, U. Grey region: uncertainty in the analytical parabolic profile for laminar flow from Eq. (6), due to the uncertainty in the measured pressure gradient at $Re = 1800$ (approximately ± 10%). The y–axis corresponds to the vertical distance from the bottom of the pipe, y, normalised by the pipe diameter, D.

$$v_{\mathrm{rms}} = \sqrt{\frac{1}{n-1}\sum_{i=1}^{n}(v_i - \langle v \rangle)^2}, \tag{4}$$

$$\langle u'v' \rangle = \frac{1}{n-1}\sum_{i=1}^{n}(u_i - \langle u \rangle)(v_i - \langle v \rangle)\ . \tag{5}$$

3. Results and discussion

Measurement data on in situ interface levels, mean and rms velocity profiles, and Reynolds stress profiles are presented in this section from the application of the aforementioned two–line PLIF–PIV/PTV technique to the horizontal stratified and stratified–wavy oil–water pipe flows established in the TOWER facility over the range of conditions stated in Table 2.

3.1. Single–phase flow

A single–phase laminar–flow investigation was conducted in order to validate the experimental methodology. The mean axial velocity profile constructed from the PTV vector map was compared with the analytical (parabolic) solution for laminar flow in circular pipes:

$$u(r) = -\frac{R^2}{4\mu}\frac{\Delta P}{\Delta L}\left(1 - \frac{r^2}{R^2}\right), \tag{6}$$

where r is the distance from the pipe centreline, R is the pipe radius, μ is the oil viscosity, and $\Delta P/\Delta L$ is the experimentally–measured pressure gradient.

A comparison of the experimentally–derived axial velocity profile at $Re = 1800$ (low flow–rate, single–phase oil flow) and the profile constructed from Eq. (6) shows good agreement (see Fig. 6). In particular, the measured velocity profile falls within the uncertainty region of the analytical velocity profile of approximately ± 10% due to the (dominant) uncertainty in the measured pressure gradient in Eq. (6), shown as the grey region in Fig. 6. The vertical velocity shows a small negative component with a fairly symmetric profile with respect to the pipe centreline. This profile, in the laminar flow regime, is in agreement with those observed in oil–water flows (in the oil phase for $Re < 2000$) as presented in Section 3.3.

3.2. In situ interface level

Instantaneous in situ (local) water–layer height values, h_w, were extracted from the PLIF images. Fig. 7a shows the time–averaged in situ water–layer (interface) height, $\langle h_w \rangle$, over the entire set of images in each tested condition. For a given mixture velocity, U_m, the water layer height increases with the water cut, WC, as expected. At the lowest WC of 5% the mean height is found in a narrow band at 0.08–0.09 D (≈3 mm) from the bottom of the pipe. At the higher WC of 10% the mean height rises to 0.16–0.17 D (≈5 mm). In these results, U_m has no discernible effect on the mean interface height. At the highest tested WC of 20%, a decrease in the mean interface height by up to ≈20% from 0.30 D to 0.26 D (10 to 8 mm) can be seen as U_m increases.

When interpreting the results in Fig. 7a, which relate to the interface height in a central vertical plane along the pipe/flow axis, it is important to consider also the three–dimensional nature of the interface. Direct observations revealed that the interface has a slight curvature in the vertical plane, especially close to the pipe walls, exhibiting a convex profile (i.e., water wets the pipe). This profile curvature was expected and is known to increase at higher mixture velocities and water holdups. Specifically, Ng et al., (2001) developed a model to predict the interface curvature in laminar stratified liquid–liquid flows in circular pipes based on the contact angle θ between the pipe material and test fluids, and the Bond number, $Bo = \Delta\rho g D^2/4\gamma$, where g is the gravitational acceleration, and $\Delta\rho$ is the water–oil density difference. This model predicts a relatively flat interface for the current system and in situ water fractions lower than 30%.

Information on the fluctuation rms of the interface (height) profile, shown in Fig. 7b, indicates that the amplitude of the interfacial waves increases with the mixture velocity to a maximum at $U_m = 0.5$ m/s. Inspection of the temporal evolution of the interface, shown in Fig. 8, reveals two behaviours: (1) low–frequency waves (i.e., long wavelengths) with local waves of low amplitude, which are more prominent at low mixture velocities (see, e.g., $U_m = 0.4$ m/s); and (2) high–frequency waves which are more prominent at high mixture velocities (see, e.g., $U_m = 0.6$ m/s). For the flow at $U_m = 0.5$ m/s, the interface exhibits characteristics of both aforementioned behaviours resulting in larger rms values, whereas the higher speed flow at $U_m = 0.6$ m/s has a reduced long–wavelength content but increased high–frequency amplitudes. This interfacial behaviour is also expected to affect the structure of the flow (e.g., axial and vertical velocities), which are presented in the following sections.

A further statistical analysis has also been performed on the temporal evolution of the interface for the flow conditions shown in Fig. 8. Integral time–scales, from autocorrelation functions, were obtained to characterise the temporal evolution of the interface and to calculate unbiased estimators of the mean and standard deviation of the interface height and fluctuation. The unbiased estimators, which were based on samples separated by 2 integral time–scales, were also compared to estimators from all samples over the entire sampling time, shown in Fig. 7. The integral times for $U_m = 0.4$, 0.5, and 0.6 m/s are 0.24, 0.17, and 0.08 s, respectively, which offers further insight into to the long– and short–wavelength observations at $U_m = 0.5$ and 0.6 m/s. The average absolute deviations (AADs) between the two estimators for the mean and rms of the interface height are 1.2% and 4.7%, respectively, which is considered within the experimental error of the present work. Furthermore, power spectral density (PSD) profiles at $WC = 20\%$ for different mixture velocities are presented in Fig. 9. These confirm the observations stated above. For $U_m = 0.4$ m/s, the PSD shows the lowest power level at all frequencies indicating minimum interface wave activity. At higher mixture velocities, two

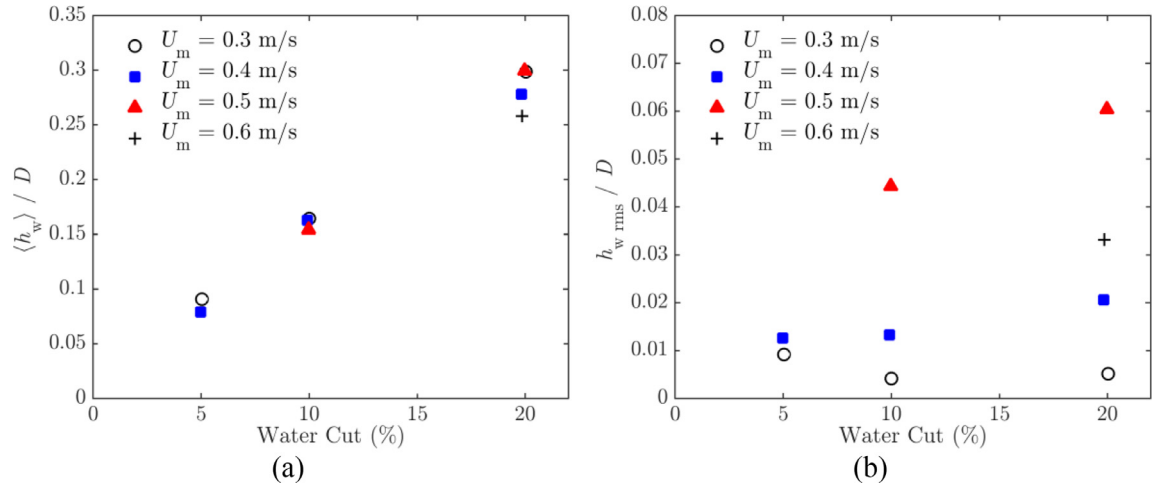

Fig. 7. (a) Time–averaged water layer height (interface level) relative to the bottom of the pipe, $\langle h_w \rangle$, and (b) interface height fluctuation or rms normalised by the pipe diameter, D, as a function of water cut, WC, for different mixture velocities, U_m.

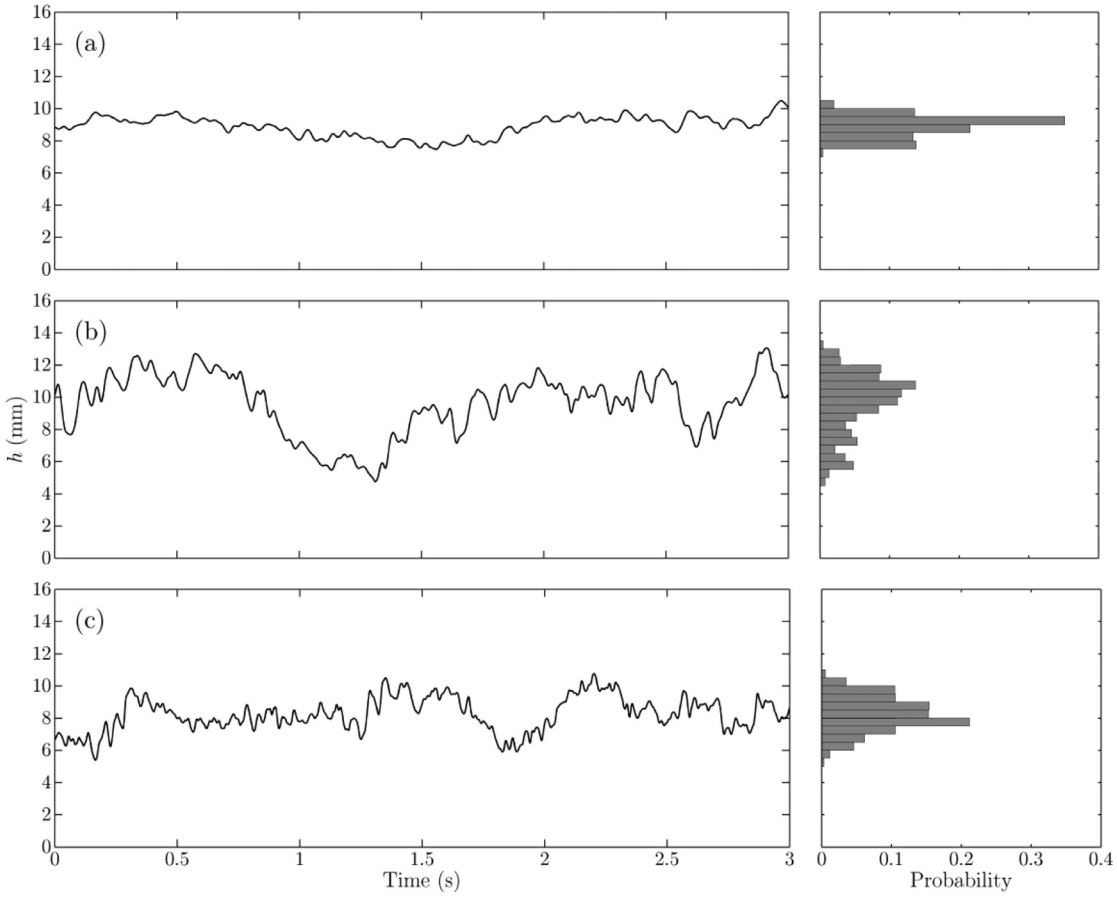

Fig. 8. Temporal evolution of the interface and probability histograms for $WC = 20\%$ and mixture velocities of: (a) $U_m = 0.4$ m/s, (b) $U_m = 0.5$ m/s, and (c) $U_m = 0.6$ m/s.

different trends are observed: higher power for $U_m = 0.5$ m/s at low frequencies and collapsed profiles at higher frequencies.

3.3. Flow structures and velocity profiles

Instantaneous velocity fields can provide insight into the different flow structures encountered in the oil–water flow system of interest. Examples of such fields can be seen in Fig. 10 for two different flow configurations: smooth interface with fairly parallel streamlines in the oil phase (small velocity fluctuations), and wavy interface with a non–uniform velocity distribution in both phases (large velocity fluctuations). This figure shows instantaneous velocity vectors (with the axial velocity magnitude indicated by the background colour) and corresponding local axial velocity profiles, $u(y)$, at two different streamwise positions, x, and corresponding spatially–averaged instantaneous axial velocity profiles, $\langle u \rangle_x$, for flows with conditions: $WC = 20\%$, and $U_m = 0.3$ and 0.6 m/s.

The axial velocity profile appears smooth without notable features at low mixture velocities ($U_m = 0.3$ m/s) for which a generally flat interface is observed. Local axial velocity profiles at two

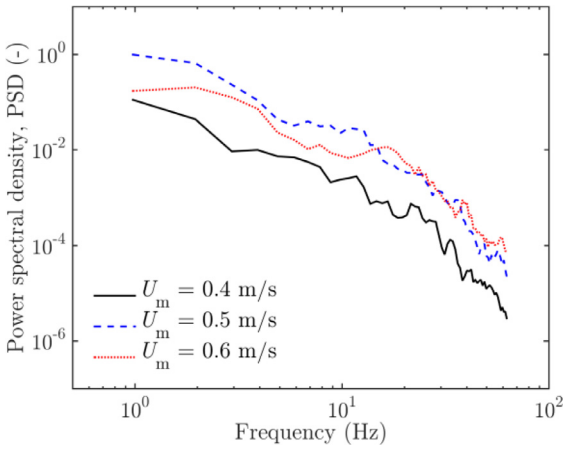

Fig. 9. Interface temporal evolution PSD for different mixture velocities, U_m, and $WC = 20\%$.

different streamwise positions show very similar profiles, especially in the oil layer, resulting in low velocity fluctuation rms values (shown as the error bar in the spatially–averaged instantaneous axial velocity profiles, $\langle u \rangle_x$) in the oil layer. With increasing U_m, and therefore Re_{oil} and Re_w, more complex velocity structures gradually appear in the flow field, as the axial velocity profiles begin to show unsteadiness resulting in an increase in the velocity fluctuations. This is also observed in the rms velocity fluctuation profiles discussed in the next section.

Mean (time–averaged) axial velocity profiles, $\langle u \rangle$, and mean vertical velocity profiles, $\langle v \rangle$, have been normalised by their respective mixture velocities, U_m, to identify common trends for different flow conditions. Fig. 11 shows the normalised $\langle u \rangle / U_m$ and $\langle v \rangle / U_m$ profiles for water cuts in the range $WC = 5$–20% at a mixture velocity of $U_m = 0.3$ m/s. The mean axial profiles reflect laminar flow behaviour in the oil phase and transitional/turbulent flow behaviour in the water phase. This is consistent with expectations from the in situ Reynolds number values given in Table 2 for these flows, although it is noted that this only provides an approximate indication based on single–phase pipe flows which, generally, can exhibit turbulence characteristics for Reynolds numbers above 2000. In two–phase flow systems, the flow is destabilised by the presence of an interface, with unstable 'interfacial modes' appearing due to viscosity–stratification at arbitrary small Reynolds numbers (Yih, 1967; Yiantsios and Higgins, 1988; Náraigh et al., 2011).

The normalised mean axial velocity profiles collapse in the oil phase, with the exception of the profile associated with the lowest water cut, $WC = 5\%$. The normalised mean vertical velocity profiles show negative values in the oil phase for the cases studied, meaning that the oil phase flows towards the interface, with a vertical of velocity component that appears to be relatively uniform over y/D and a pronounced peak at the interface in the $WC = 20\%$ flow case. Similarly, the water phase flows towards the bottom of the pipe, except for the $WC = 5\%$ flow case, for which there is a near–zero vertical flow component. These observations indicate that sec-

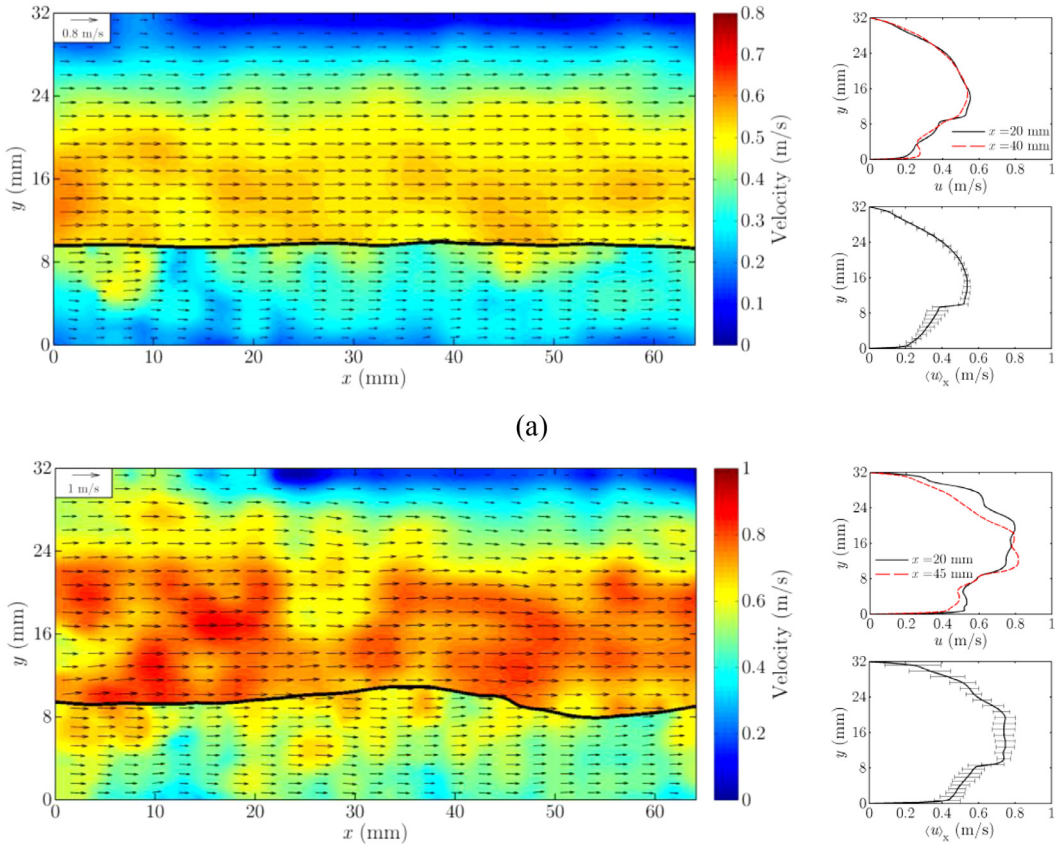

Fig. 10. Instantaneous velocity fields (the axial velocity magnitude is indicated by the colour–plot, and the interface profile by the black solid line), with corresponding local axial velocity profiles, $u(y)$, and spatially–averaged axial velocity profiles, $\langle u \rangle_x(y)$, for $WC = 20\%$ and mixture velocities of: (a) $U_m = 0.3$ m/s ($Re_{oil} = 1850$, $Re_w = 5820$), and (b) $U_m = 0.6$ m/s ($Re_{oil} = 3350$, $Re_w = 11{,}650$). The vertical distance, y, is measured from the bottom of the pipe. The error bars in the $\langle u \rangle_x$ profiles indicate the local axial velocity rms, not the experimental error (for ease of visualisation not all vectors are shown in the velocity fields).

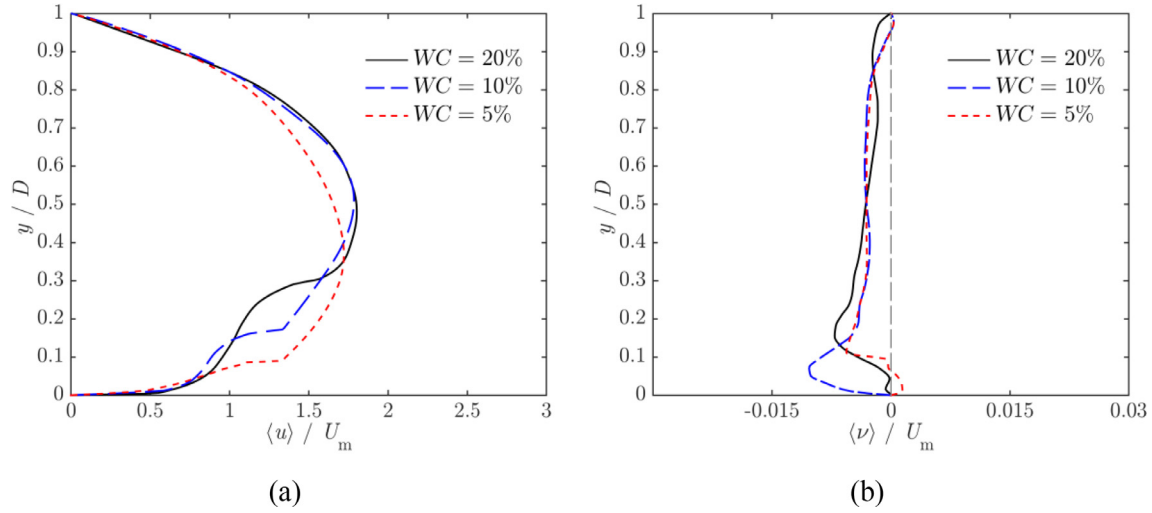

Fig. 11. Normalised mean: (a) axial velocity profiles, and (b) vertical velocity profiles, at different water cuts for $U_m = 0.3$ m/s ($Re_{oil} = 1750$, $Re_w = 2860$ for $WC = 5\%$; $Re_{oil} = 1810$, $Re_w = 4140$ for $WC = 10\%$; $Re_{oil} = 1850$, $Re_w = 5820$ for $WC = 20\%$). The in situ interface positions for all flows can be found in Fig. 7, and these generally match the velocity gradient discontinuities at $y/D \approx 0.08$–0.09, 0.16–0.17, 0.26–0.30 for $WC = 5$, 10, 20%, respectively.

ondary flows are present in the system, as will be described in Section 3.4.

It is expected that increased vertical velocity gradients will act to transfer momentum over the flow section, and that this will manifest itself in the shapes of the various profiles. Consider Fig. 12 for $U_m = 0.4$ m/s. In Fig. 12a, the mean axial velocity profiles in the oil phase for $WC = 5\%$ and 10% have a maximum at a location that has been shifted from the central region of the pipe to a region just above the liquid–liquid interface. This is at odds with the shape of the mean axial velocity profile observed at the other flow condition ($WC = 20\%$), where the maximum velocity is encountered near the centre of the pipe. This can be considered in light of the corresponding mean vertical velocity profiles in Fig. 12c, which indicate faster oil flows towards the interface for $WC = 5$ and 10% in comparison to $WC = 20\%$ and suggest that significant vertical momentum is transferred downwards, and towards the interface region.

From inspection of Fig. 12d, which includes all flow cases with $WC = 10\%$, we see that for the lower-speed flows ($U_m \leq 0.4$ m/s) in the laminar/transitional regimes ($Re_{oil} \leq 2400$), the mean vertical velocity component shows negative values in the oil phase, which therefore flows downward towards the interface. Above this velocity ($U_m = 0.5$ m/s, $Re_{oil} = 2860$), the flow reverses and moves upward in the core region the oil phase. This behaviour has not been observed in previous studies, which have generally considered flow conditions with Reynolds numbers either in the fully laminar or fully turbulent regimes (e.g., Kumara et al., 2010; Amundsen, 2011; Morgan et al., 2013). The same pattern can also be observed for $WC = 20\%$ at different mixture velocities, as presented in Fig. 13, although the vertical velocity in the oil phase for $Re_{oil} < 2300$ has a weaker downwards flow component (reduced negative values) compared to the lower WC case (compare Figs. 12d and 13b), which may be attributed to the restricted oil layer cross-section flow area. This, in turn, is not strong enough to modify the shape of the mean axial profile, so the mean axial velocity profiles exhibit maximum values in the central region of the pipe, as shown in Fig. 13a. The normalised mean axial velocity profiles for $WC = 20\%$, collapse in the water layer at the bottom section of the pipe, over all U_m values studied and for which $Re_w > 4000$ (see Table 2).

3.4. Secondary flow structures

Although our investigated liquid–liquid stratified flows are three-dimensional in nature, an attempt is made here to shed some light on any underlying secondary flow structures present in these flows within the limits of our two-dimensional experimental approach, based on the observations from the profiles of $\langle u \rangle$ and $\langle \nu \rangle$ shown in Figs. 12 and 13. Secondary flows can be produced by interfacial interactions and boundary-layer effects. In particular, surface waves are believed to contribute to the generation of secondary flow structures in two-phase flows (Nordsveen, 2001). Liné et al., (1996) studied the structure of these flows in stratified gas–liquid systems in rectangular channels, and observed that the flows in both phases have a significant effect on the spatial distribution of the axial velocity component and interfacial shear stress. Conan et al., (2007) examined horizontal and vertical radial velocity profiles (passing through the centreline of the pipe) in order to study secondary flow structures in stratified-dispersed liquid–liquid flows with matched refractive-index fluids. They deduced two symmetrical pairs of counter-rotating vortices in the bottom continuous aqueous (water–glycerol solution) layer and concluded that the non-uniform turbulent kinetic energy along the fluid–pipe perimeter of the continuous phase could be responsible for the generation of secondary flows in stratified-dispersed flows. Further, Belt et al., (2012) used laser droplet anemometry to study secondary flows in single-phase water in horizontal pipes with fixed particles at the bottom section, which, however, modifies the small-scales of the flow, especially around the particles, leading to non-uniformity in the Reynolds stress tensor and generating secondary flows.

The vertical velocity profiles in the measurement plane (see Figs. 11–13) together with continuity arguments indicate that secondary flows exist, and it is possible to some extent to deduce secondary flow structures at different flow conditions, at least qualitatively. Negative (positive) vertical velocities indicate downwards (upwards) flows, as explained above, and symmetry can be assumed in each phase about the vertical axis leading to pairs of counter-rotating vortices in either phase, above and below the interface. This leads to a range of possible secondary flows from single-vortex in each layer to more complex two or three counter-rotating vortices in each layer. Although it is not possible based on present data alone to report definitely on these flow phenomena, the occurrence and detailed characteristics of such secondary flow structures could be confirmed by horizontal velocity profiles, ideally, at different horizontal planes.

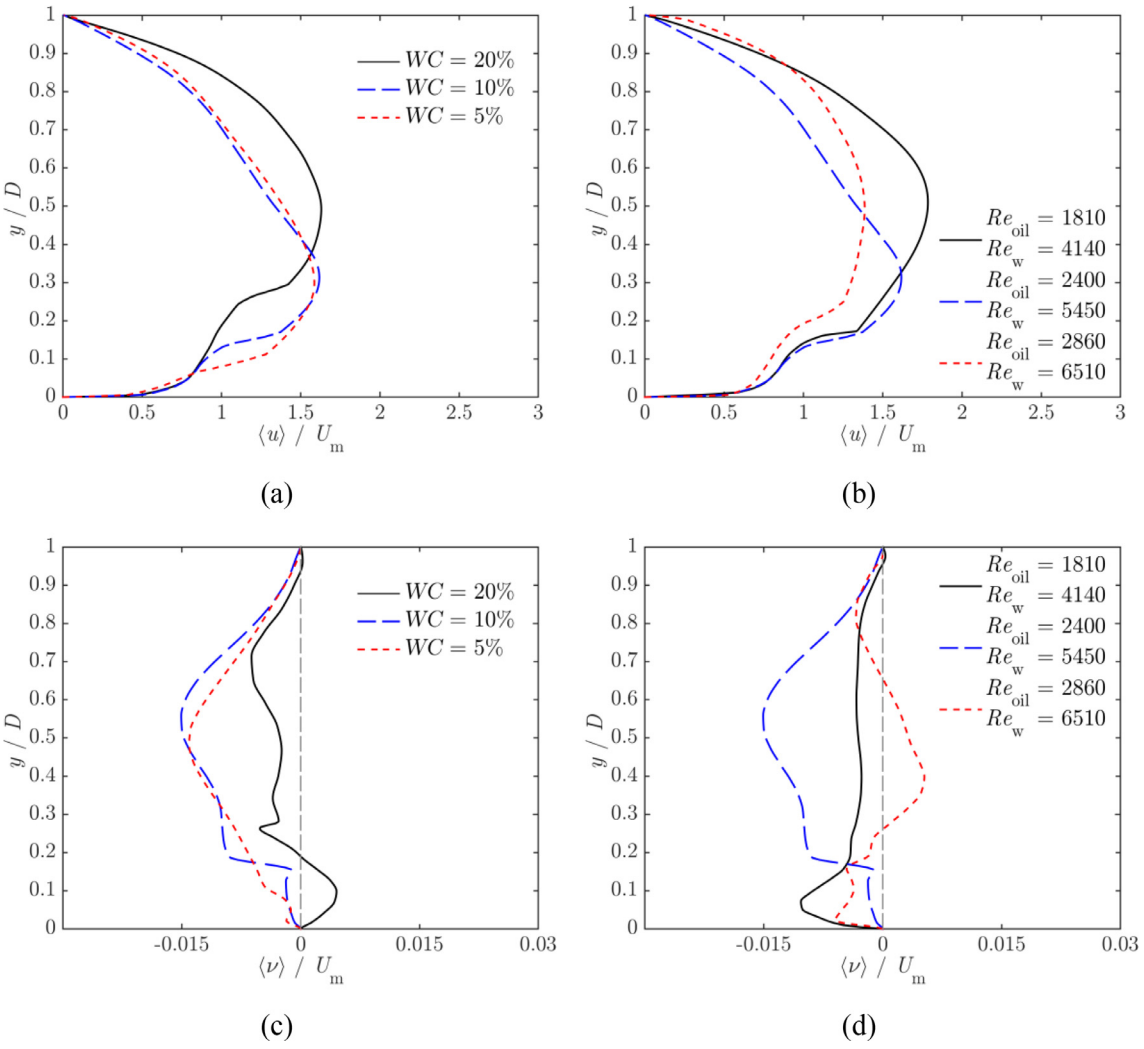

Fig. 12. Normalised mean axial (a) and (b) and vertical (c) and (d) velocity profiles, at different WC with $U_m = 0.4$ m/s (a) and (c), and different U_m with $WC = 10\%$ (b) and (d).

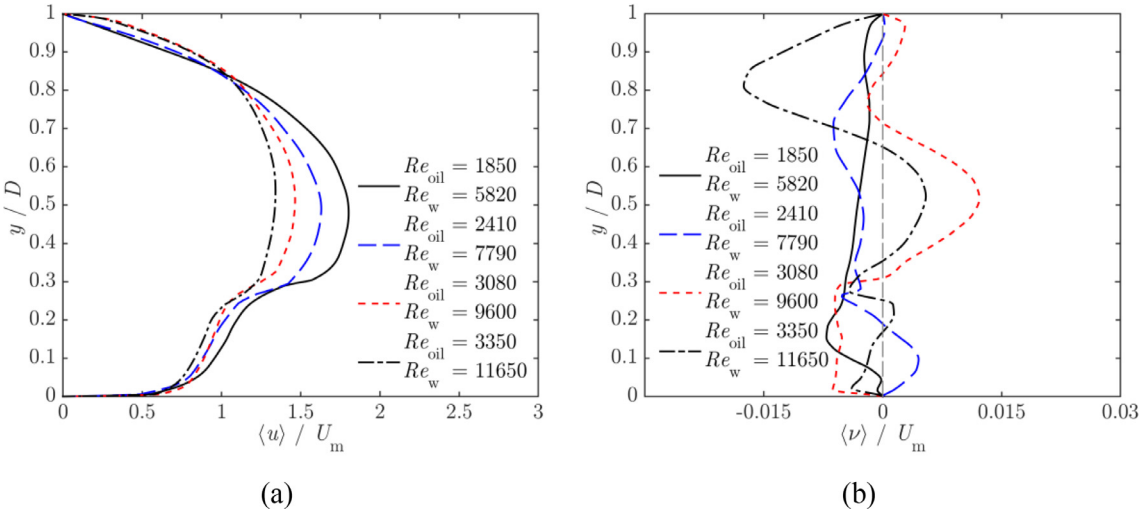

Fig. 13. Normalised mean: (a) axial, and (b) vertical velocity profile at different mixture velocities, U_m, and $WC = 20\%$.

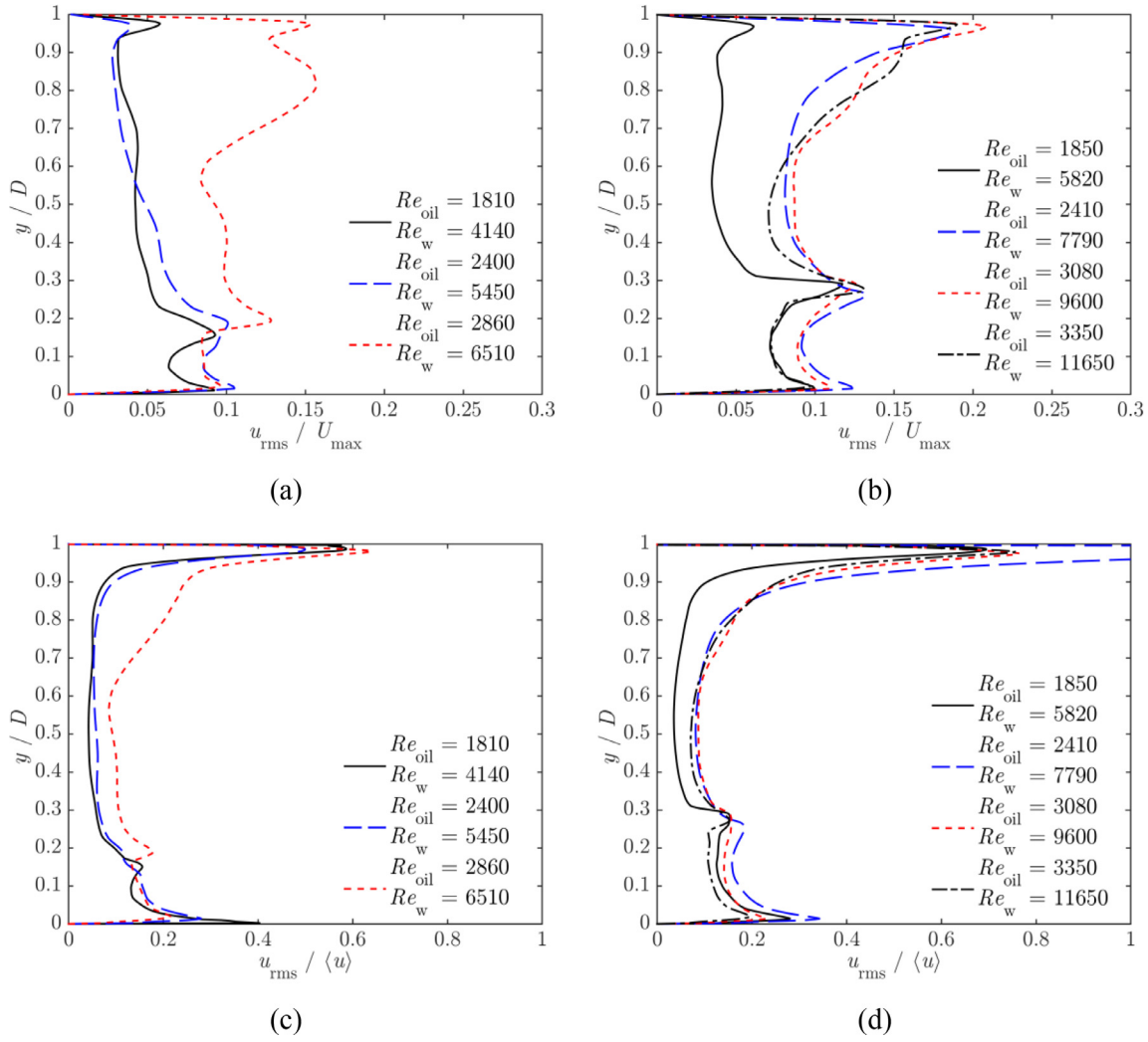

Fig. 14. Axial turbulence intensity at different *Re*, or U_m, and a *WC* of: (a) and (c) 10%, and (b) and (d) 20%, normalised by the peak mean velocity, U_{max}, (a), (b) and local mean axial velocity, $\langle u \rangle$ (c), (d).

3.5. Flow unsteadiness

The level of flow unsteadiness can be characterised via the quantification of the velocity fluctuation rms in the axial, u_{rms}, and vertical directions, v_{rms}. In single–phase pipe flows, peaks are observed near the pipe wall due to high shear in this region of the flow. The velocity fluctuations then decrease towards the centre of the pipe to a minimum value where the mean velocity gradient is zero. This has been observed by Amundsen (2011) and Kolaas et al., (2015) by the implementation of LDA and PIV/PTV, respectively.

In our flows, an additional peak is observed in the velocity fluctuations in the near–interface region. Fig. 14 shows the axial turbulence intensity, or rms of the axial velocity fluctuation, u_{rms}, normalised by the respective peak mean axial velocity (see Figs. 12 and 13 for U_{max}), and by the local mean axial velocity, $\langle u \rangle$, at different U_m and for $WC = 10$ and 20%. Peaks appear close to the pipe wall and near the interface, and minimum values in the bulk of each phase. The normalisation of u_{rms} collapses the data to some extent at the bottom section of the pipe (to a value of ≈10%), which corresponds to the water layer. This may suggest that the water flow is generally turbulent, and that u_{rms} scales reasonably well with U_{max} and $\langle u \rangle$. In the oil phase, we can see a marked increase in the turbulence intensity as U_m increases from low values and a collapse at higher U_m (also at ≈10%), perhaps due to transition from laminar to turbulent flow for $Re_{oil} > 2300$–2400.

Fig. 15 shows profiles of the vertical turbulence intensity, or normalised rms of the vertical velocity fluctuations, v_{rms}, at different U_m and $WC = 10$ and 20%. The profiles show similar characteristics to those observed for the axial turbulence intensity, with peaks near the pipe wall and interface. However, for $U_m \geq 0.5$ m/s ($Re_{oil} \geq 2860$ and $Re_{oil} \geq 3080$ for $WC = 10$ and 20%, respectively) an additional region of high turbulence intensity appears in the bulk of the oil layer. It is hypothesised that this may be linked to the large velocity gradients that arise due to the presence of counter–rotating vortices in the flow (secondary flow structures), which would be expected to increase the shear in the flow.

The momentum flux term $\langle u'v' \rangle$, also referred to as the Reynolds stress, has also been considered. Fig. 16 shows the Reynolds stress $\langle u'v' \rangle$ normalised by the corresponding mixture velocity, U_m, for different flows with $WC = 20\%$. In laminar flows, little mixing is expected, leading to a zero Reynolds stress, as is observed in Fig. 16 in the oil layer when $Re_{oil} \leq 2400$ and $Re_{oil} < 2000$ for $WC = 10$ and 20%, respectively. In single–phase flows, the magnitude of the Reynolds stress shows peak values at similar distances from the bottom and top of the pipe, and decreases to zero towards the centre of the pipe, with a symmetric profile with respect to the pipe axial centreline.

In the stratified two–phase flows investigated here, the Reynolds stress maximum in the water layer is located close to the bottom of the pipe while in the oil layer it is further away from

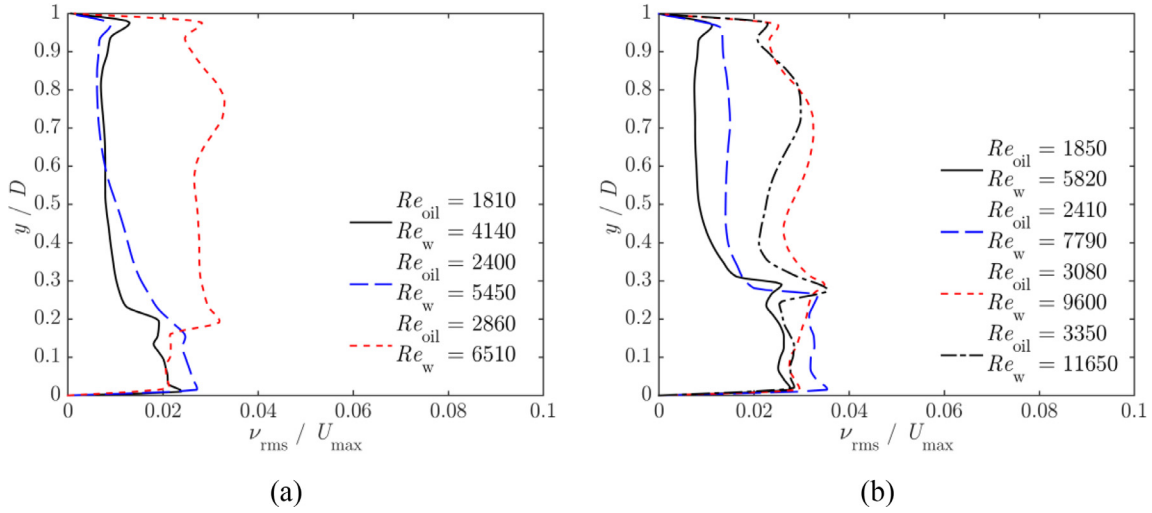

Fig. 15. Vertical turbulence intensity at different *Re*, or U_m, and a *WC* of: (a) 10%, and (b) 20%.

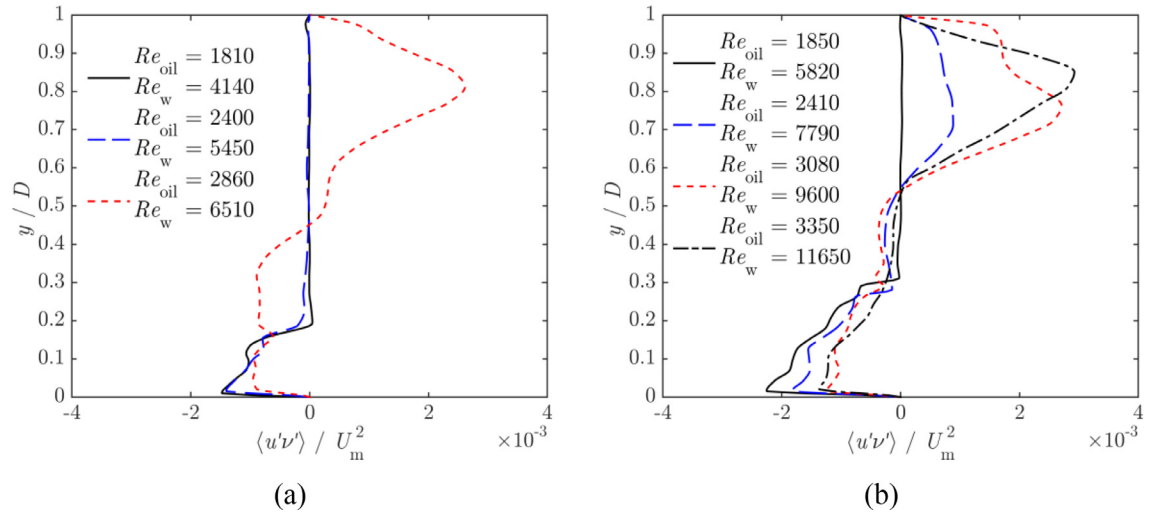

Fig. 16. Reynolds stress $\langle u'v' \rangle$ normalised by the square of the corresponding mixture velocity, U_m, at different *Re*, or U_m, and a *WC* of: (a) 10%, and (b) 20%.

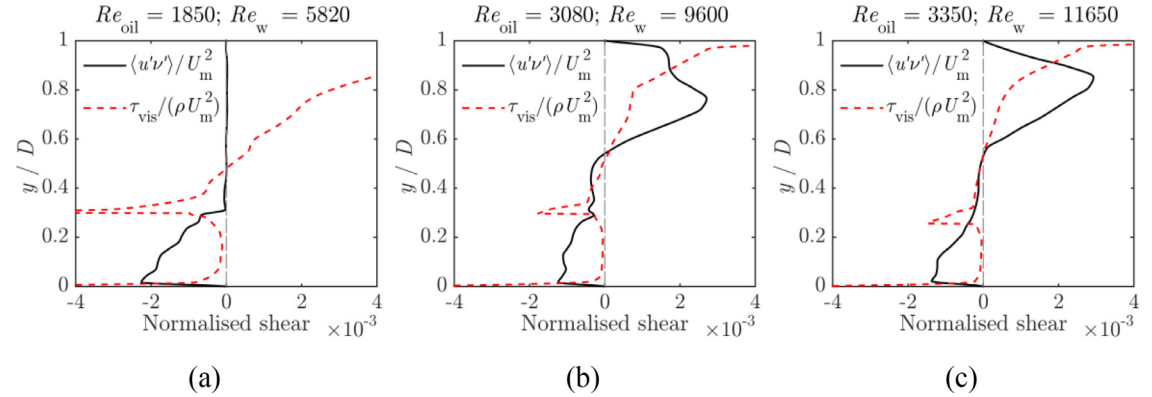

Fig. 17. (a–c) Comparison of the Reynolds stress, $\langle u'v' \rangle$, and viscous shear–stress, $\tau_{vis} = -\mu \partial \langle u \rangle / \partial y$, normalised by the square of the mixture velocity, U_m, at different *Re*, or U_m, and $WC = 20\%$.

the top wall of the pipe. The normalised Reynolds stress profiles appear to collapse to some extent in the water layer, whereas in the oil layer the Reynolds we can see a sharp increase from zero to a collapse at higher U_m. This observation is closely aligned with that made earlier in relation to the turbulence intensities, linked to a transition from laminar to turbulent flow in the oil phase.

Fig. 17 shows a comparison of the Reynolds stress, $\langle u'v' \rangle$, and the viscous shear–stress, defined as $\tau_{vis} = -\mu \partial \langle u \rangle / \partial y$. The viscous stress is dominant in the oil phase for Reynolds numbers in the laminar regime (i.e., $Re_{oil} < 2000$) where the Reynolds stress $\langle u'v' \rangle$ is zero. As Re_{oil} increases, the influence of the viscous shear in the bulk of the oil phase decreases showing only large values at the

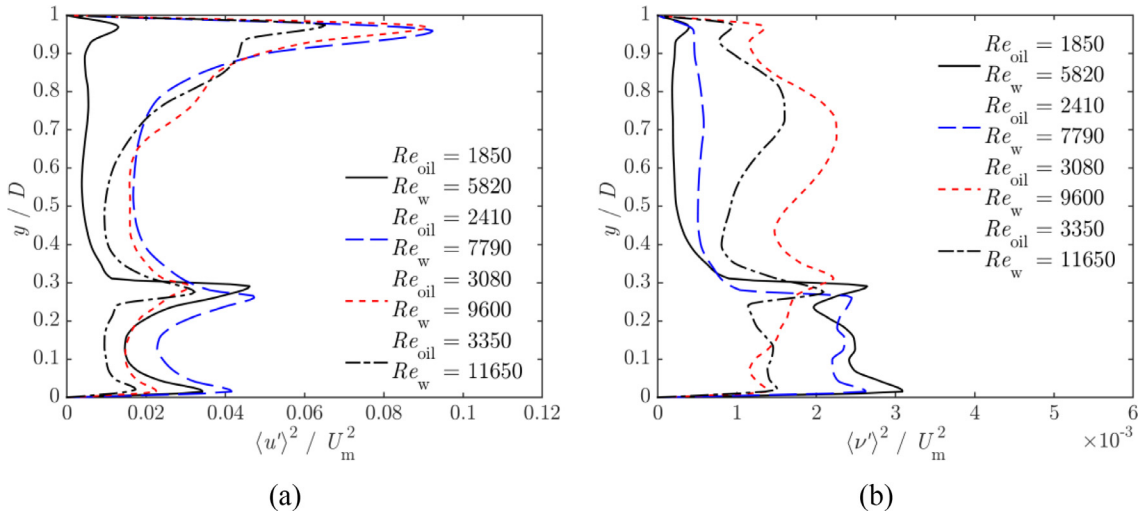

Fig. 18. (a) Axial, and (b) vertical normal stresses normalised by the square of the mixture velocity, U_m, at different Re, or U_m, and $WC = 20\%$.

pipe–wall and interface region (boundary layers). Note that the viscous shear in the bulk of the water phase has nearly no influence in the flow for all the studied conditions for which $Re_w > 5000$ (turbulent regime).

The axial and vertical Reynolds normal stresses can offer additional information regarding the level of turbulence in the flow to further analyse the occurrence of secondary flows, especially in the bulk of the oil layer. Fig. 18 shows the axial, $\langle u'^2 \rangle$, and vertical, $\langle v'^2 \rangle$, normal stresses normalised by the square of the corresponding mixture velocity, U_m, at $WC = 20\%$. Axial and vertical Reynolds normal stresses show a slight disturbance and a significant peak, respectively, in the bulk of the oil layer for $Re_{oil} > 3000$ which can be linked to the generation of counter–rotating vortices in the azimuthal direction. Peaks in the vertical Reynolds normal stress suggest that significant momentum flux is transferred in the vertical direction that can contribute to the generation of these secondary flows.

Some approaches to turbulence modelling require that for closure of the Reynolds–average Navier–Stokes equations, the Reynolds stresses must be determined *a priori*. A number of models have been employed for the estimation of these stresses, with a simple and popular formulation proposed by Prandtl (1925), known as the mixing length concept, relating the Reynolds stresses to the mean velocity gradient through a mixing length l_m given as:

$$-\langle u'v' \rangle = l_m^2 \left| \frac{\partial \langle u \rangle}{\partial y} \right| \frac{\partial \langle u \rangle}{\partial y}. \tag{7}$$

Prandtl assumed that the mixing length varies linearly with the distance from the wall, $l_m = ky$, where k is the von Karman constant ($k = 0.41$). In the viscous sublayer, a damping effect is usually introduced to account for near–wall effects as proposed by Van Driest (1956).

In two–phase stratified flows, the shear at the liquid–liquid interface complicates the definition of the mixing length profile. Biberg (2007) developed a model that accounts for the effect of interfacial waves and momentum transfer using the original mixing–length concept. This approach was utilised by Náraigh et al., (2011) for the investigation of two–layer pressure–driven channel flow where the top (gas) and bottom (liquid) layers are turbulent and laminar, respectively. However, reported experimental data on mixing length profiles for liquid–liquid flows in horizontal circular pipes is almost inexistent.

Figs. 19 and 20 show measured mixing length profiles $l_m(y/D)$ from Eq. (7) for flows with $WC = 10$ and 20%, along with corresponding predictions based on the von Karman constant ($k = 0.41$), which are shown as straight solid lines labelled '1', '2' and '3'. Mixing length predictions have the form $l_m = nk(y - y_0)$ where coefficients n and y_0 are given in Table 3, and are functions of the mean interface height, $\langle h_w \rangle$. The mean interface height for the flow conditions in Figs. 19 and 20 is located between $y/D = 0.16$–0.17 for $WC = 10\%$ and $y/D = 0.26$–0.30 for $WC = 20\%$, depending on the flow condition (see Fig. 7).

Table 3
Coefficients for the mixing length prediction approach.

Model	n	y_0
1	1	0
2	−1	$\langle h_w \rangle$
3	1	$\langle h_w \rangle + 0.07D$

At the bottom region of the pipe (water layer), measured mixing length profiles can be modelled using the standard expression of the mixing length concept (i.e., $l_m = ky$) until the vertical distance (from the pipe bottom) which corresponds to the inflection point in the mean axial velocity profile in the water layer. Above this point, the mixing length decreases towards the liquid–liquid interface where a local minimum is observed. Above the interface, the mixing length model (labelled '3' with coefficients $n = 1$ and $y_0 = \langle h_w \rangle + 0.07D$) again provides a reasonable prediction of the measured mixing length. This represents an interesting finding as the flow is expected to be laminar/transitional in the oil phase ($Re_{oil} < 4000$), such that the Reynolds stresses cannot normally be modelled using this concept; at the top of the pipe, in the region above $y(\partial \langle u \rangle / \partial y = 0)$, the mixing length profiles show significantly different behaviour.

3.6. Velocity field normalisation

The mean and rms velocity profiles presented in earlier sections were constructed from instantaneous velocity fields by considering statistics at each position y away from the bottom wall of the pipe and ignoring the interface. This means that in fluctuating interfacial regions these quantities will include information from both the oil and water phases. An alternative analysis can be performed, which is also commonly employed in reduced–order modelling of these flows, by normalising the local and instantaneous interface height with respect to the mean interface height, $\langle h_w \rangle$; this transforms the flow fields from having a wavy interface to a flat one

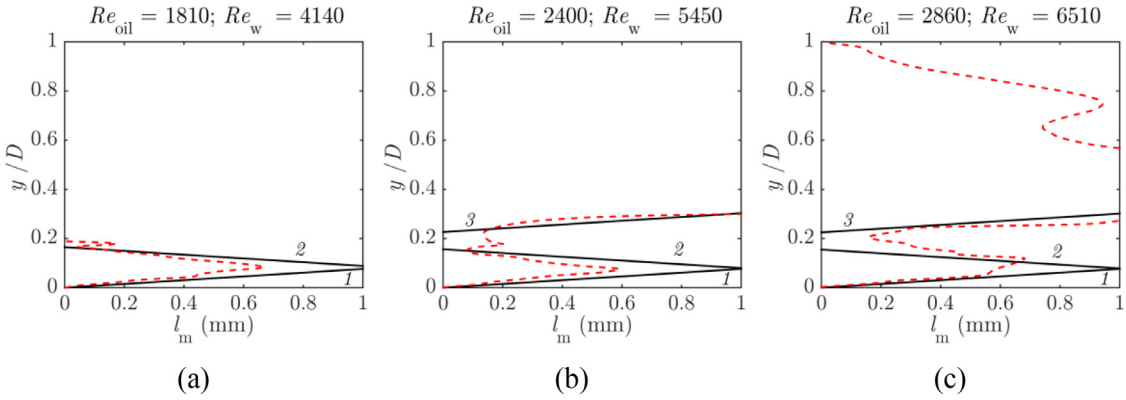

Fig. 19. Mixing length profiles for different *Re*, or U_m, at $WC = 10\%$, and predictions based on the von Karman constant ($k = 0.41$) shown as the black solid lines '1', '2' and '3'.

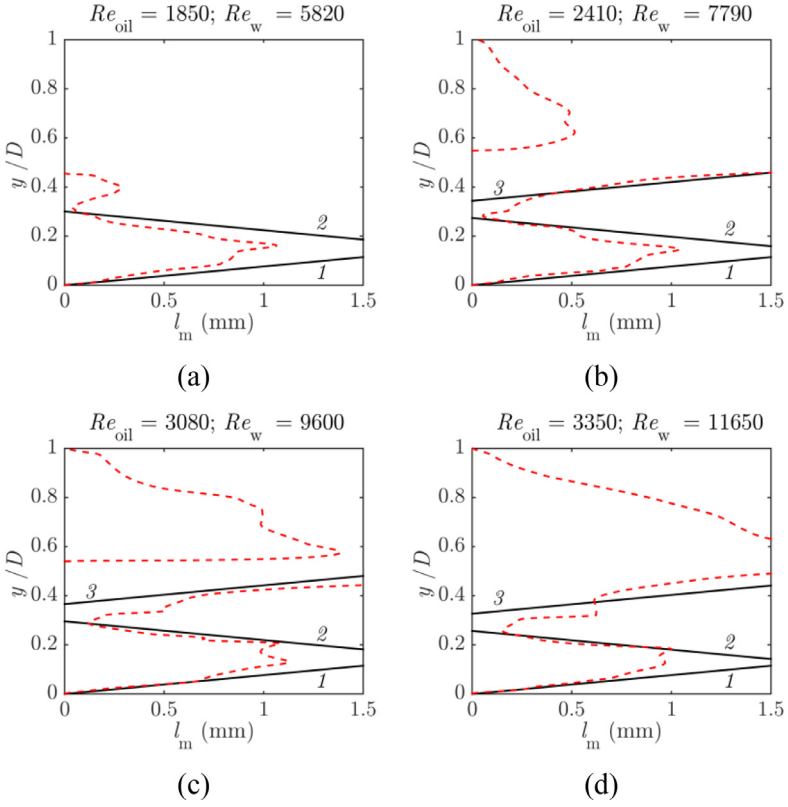

Fig. 20. Mixing length profiles for different *Re*, or U_m, at $WC = 20\%$, and predictions based on the von Karman constant ($k = 0.41$) shown as the black solid lines '1', '2' and '3'.

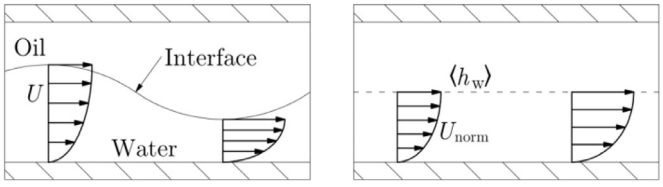

Fig. 21. Velocity field normalisation based on the mean water–layer or interface height, $\langle h_w \rangle$.

(see Fig. 21) and re–scales the velocity fields to adjust for the interface height normalisation.

Fig. 22 shows a mean axial velocity profile and profiles of the axial and vertical rms velocity fluctuations constructed from normalised instantaneous velocity fields for a selected flow with $U_m = 0.6$ m/s and $WC = 20\%$, and a comparison with equivalent results shown earlier generated without employing this practice of normalisation. The mean velocity profile shows a sharper gradient and the velocity fluctuations appear enhanced in the near interface region when based on normalised velocity field data, which justifies attempts to add turbulence source terms at the interface in modelling frameworks that employ such a normalisation. Conservation of mass can be accounted for to ensure this balances in the revised velocity distributions, however, this requires knowledge of the out–of–plane velocity component. Although this may be assumed small relative to the axial velocity component, it is not pursued further in the present work.

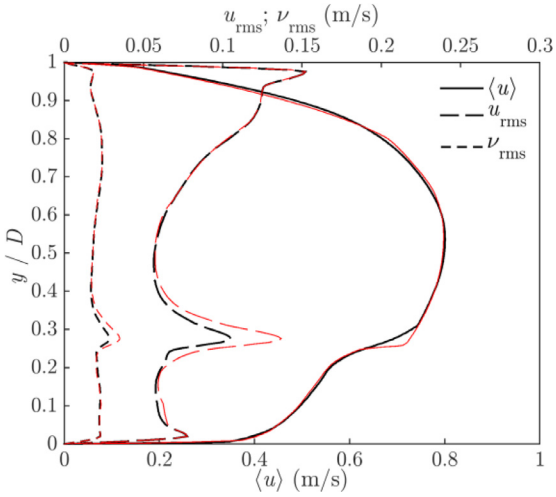

Fig. 22. Comparison of the mean axial velocity profile, $\langle u \rangle$, and axial, u_{rms}, and vertical, ν_{rms}, rms velocity fluctuations between the non–normalised (black thick lines) and normalised (red thin lines) velocity fields based the mean interface height, $\langle h_w \rangle$, for $U_m = 0.6$ m/s and $WC = 20\%$. (For interpretation of the references to colour in this figure legend, the reader is referred to the web version of this article.)

4. Conclusions

Experiments were conducted in a 32–mm ID horizontal pipe to study the hydrodynamics of stratified oil–water flows. A two–line (two–colour) laser–based diagnostic technique based on planar laser–induced fluorescence combined simultaneously with particle image/tracking velocimetry was developed and employed to obtain detailed, spatiotemporally–resolved in situ flow (phase, velocity) information in a vertical plane along the pipe centreline, and extending across the entire height of the channel through both phases. This system allows the simultaneous study of two–phase liquid–liquid flows for fluids with different refractive indices, however, the technique is limited, generally, to separated flows (i.e., stratified or stratified–wavy flows) as the presence of droplets of one phase in the bulk of the other act to distort the incident laser light, as well as the scattered and fluorescence signals, gradually reducing the accuracy of the obtained information as the complexity of the mixing increases. The resulting data were analysed to provide statistical in situ information on interface levels, mean axial and radial (vertical) velocities, (rms) velocity fluctuations, Reynolds stresses and mixing lengths.

The resulting mean velocity profiles show characteristics of both laminar and turbulent flow for the conditions studied and interesting interactions between the two co–flowing phases. Normalised velocity profiles show that the mean axial velocity in the water phase is independent of the mixture velocity for a given water cut. Evidence suggests that vertical velocity components can modify the shape of the axial velocity profile especially in transitional flows, resulting in a particular near–parabolic mean axial profile where the maximum velocity is shifted away (here, downwards) from the central region of the pipe. The level of unsteadiness in the flow was characterised by the velocity fluctuation rms and Reynolds stresses. The former showed peaks in regions of high shear, i.e., close to the pipe wall and at the liquid–liquid interface. An additional region of high shear was observed inside the bulk of the oil layer, perhaps generated by the formation of counter–rotating vortices, i.e., secondary flow structures in the flow. The axial turbulence intensity (defined relative to the peak mean axial velocity) in the bulk of the water layer was about 10% for the studied flow conditions. In the oil phase the axial turbulence intensity increased with U_m from low values and collapsed at higher U_m, again to about 10%, perhaps due to transitional flow at $Re_{oil} \approx 2300–2400$. Similar observations were made for the Reynolds stresses. Finally, the Reynolds stresses and mean axial velocity gradients were used to generate mixing length profiles. Interestingly, the development of the mixing length in the water phase and also above the liquid–liquid interface in the oil phase was found to agree reasonably well with predicted variations described by the von Karman constant.

This information can help improve our fundamental understanding of liquid–liquid flows as well as the development and validation of advanced models for the prediction of multiphase flows.

Acknowledgements

This work was undertaken within the Consortium on Transient and Complex Multiphase Flows and Flow Assurance (TMF). The authors gratefully acknowledge the contributions made to this project by the following: – ASCOMP, BP Exploration; Cameron Technology & Development; CD–adapco; Chevron; KBC (FEESA); FORSYS; INTECSEA; Institutt for Energiteknikk (IFE); Kongsberg Oil & Gas Technologies; Wood Group Kenny; Petrobras; Schlumberger Information Solutions; Shell; SINTEF; Statoil and TOTAL. The authors wish to express their sincere gratitude for this support. This work was also supported by the UK Engineering and Physical Sciences Research Council (EPSRC) [grant numbers EP/K003976/1 and EP/L020564/1]. Data supporting this publication can be obtained on request from cep-lab@imperial.ac.uk.

Supplementary materials

Supplementary material associated with this article can be found, in the online version, at doi:10.1016/j.ijmultiphaseflow.2017.12.018.

References

Amundsen, L., 2011. An Experimental Study of Oil–Water Flow in Horizontal and Inclined Pipes Ph.D. thesis. Norwegian University of Science and Technology.
Angeli, P., Hewitt, G.F., 2000. Flow structure in horizontal oil–water flow. Int. J. Multiph. Flow 26, 139–157.
Arirachakaran, S., Oglesby, K.D., Malinowsky, M.S., Shoham, O., Brill, J.P., 1989. An analysis of oil/water phenomena in horizontal pipes. In: Proceedings of the SPE Production Operations Symposium. Oklahoma City, pp. 155–167. SPE Paper 18836.
Ashwood, A.C., Vanden Hogen, S.J., Rodarte, M.A., Kopplin, C.R., Rodríguez, D.J., Hurlburt, E.T., Shedd, T.A., 2015. A multiphase, micro–scale PIV measurement technique for liquid film velocity measurements in annular two–phase flow. Int. J. Multiph. Flow 68, 27–39.
Ayati, A.A., Kolaas, J., Jensen, A., Johnson, G.W., 2014. A PIV investigation of stratified gas–liquid flow in a horizontal pipe. Int. J. Multiph. Flow 61, 129–143.
Belt, R.J., Daalmans, A.C.L., Portela, L.M., 2012. Experimental study of particle–driven secondary flow in turbulent pipe flows. J. Fluid Mech. 709, 1–36.
Biberg, D., 2007. A mathematical model for two–phase stratified turbulent duct flow. Multiph. Sci. Technol. 19, 1–48.
Birvalski, M., Tummers, M.J., Delfos, R., Henkes, R.A.W.M., 2014. PIV measurements of waves and turbulence in stratified horizontal two–phase pipe flow. Int. J. Multiph. Flow 62, 161–173.
Charles, M.E., Govier, G.W., Hodgson, G.W., 1961. The horizontal pipeline flow of equal density oil–water mixtures. Can. J. Chem. Eng. 39, 27–36.
Charogiannis, A., An, J.S., Markides, C.N., 2015. A simultaneous planar laser–induced fluorescence, particle image velocimetry and particle tracking velocimetry technique for the investigation of thin liquid–film flows. Exp. Thermal Fluid Sci. 68, 516–536.
Conan, C., Masbernat, O., Decarre, S., Line, A., 2007. Local hydrodynamics in a dispersed–stratified liquid–liquid pipe flow. AIChE 53, 2754–2768.
Elsinga, G.E., Ganapathisubramani, B., 2013. Advances in 3D velocimetry. Meas. Sci. Technol. 24, 020301.
Ibarra, R., Markides, C.N., Matar, O.K., 2014. A review of liquid–liquid flow patterns in horizontal and slightly inclined pipes. Multiph. Sci. Technol. 26, 171–198.
Ibarra, R., Zadrazil, I., Markides, C.N., Matar, O.K., 2015. Towards a universal dimensionless map of flow regime transitions in horizontal liquid–liquid flows. In: Proceedings of the Eleventh International Conference on Heat Transfer, Fluid Mechanics and Thermodynamics (HEFAT 2015). South Africa 20–23 July 2015.
Katz, J., Sheng, J., 2010. Applications of holography in fluid mechanics and particle dynamics. Annu. Rev. Fluid Mech. 42, 531–555.

Kolaas, J., Drazen, D., Jensen, A., 2015. Lagrangian measurements of two–phase pipe flow using combined PIV/PTV. J. Disper. Sci. Technol. 36, 1473–1482.
Kumara, W.A.S., Halvorsen, B.M., Melaaen, M.C., 2010. Particle image velocimetry for characterizing the flow structure of oil–water flow in horizontal and slightly inclined pipes. Chem. Eng. Sci. 65, 4332–4349.
Liné, A., Masbernat, L., Soualmia, A., 1996. Interfacial interactions and secondary flows in stratified two–phase flow. Chem. Eng. Commun. 141–142, 303–329.
Liu, L., 2005. Optical and Computational Studies of Liquid–Liquid Flows Ph.D. thesis. Imperial College London.
Markides, C.N., Mathie, R., Charogiannis, A., 2016. An experimental study of spatiotemporally resolved heat transfer in thin liquid–film flows falling over an inclined heated foil. Int. J. Heat Mass Transf. 93, 872–888.
Morgan, R.G., Markides, C.N., Hale, C.P., Hewitt, G.F., 2012. Horizontal liquid–liquid flow characteristics at low superficial velocities using laser–induced fluorescence. Int. J. Multiph. Flow 43, 101–117.
Morgan, R.G., Markides, C.N., Zadrazil, I., Hewitt, G.F., 2013. Characteristics of horizontal liquid–liquid flows in a circular pipe using simultaneous high–speed laser–induced fluorescence and particle velocimetry. Int. J. Multiph. Flow 49, 99–118.
Morgan, R.G., Ibarra, R., Zadrazil, I., Matar, O.K., Hewitt, G.F., Markides, C.N., 2017. On the role of buoyancy–driven instabilities in horizontal liquid–liquid flow. Int. J. Multiph. Flow 89, 123–135.
Morrison, G.L., Gaharan, C.A., Deotte, R.E., 1994. Doppler global velocimetry: problems and pitfalls. Flow Meas. Instrum. 6, 83–91.
O'Náraigh, L., Spelt, P.D.M., Matar, O.K., Zaki, T.A., 2011. Interfacial instability in turbulent flow over a liquid film in a channel. Int. J. Multiph. Flow 37, 812–830.
Ng, T.S., Lawrence, C.J., Hewitt, G.F., 2001. Interface shapes for two–phase laminar stratified flow in a circular pipe. Int. J. Multiph. Flow 27, 1301–1311.
Nordsveen, M., 2001. Wave– and turbulence–induced secondary currents in the liquid phase in stratified duct flow. Int. J. Multiph. Flow 27, 1555–1577.
Pouplin, A., Masbernat, O., Decarre, S., Line, A., 2015. Wall friction and effective viscosity of a homogeneous dispersed liquid–liquid flow in a horizontal pipe. AIChE 57, 1119–1131.
Prandtl, L., 1925. Report on investigation of developed turbulence. ZAMM 5, 136–139.
Russell, T.W.F., Hodgson, G.W., Govier, G.W., 1959. Horizontal pipeline flow of mixtures of oil and water. Can. J. Chem. Eng. 37, 9–17.
Schubring, D., Ashwood, A.C., Shedd, T.A., E.T., H., 2010. Planar laser–induced fluorescence (PLIF) measurements of liquid film thickness in annular flow. Part I: methods and data. Int. J. Multiph. Flow 36, 815–824.
Soleimani, A., 1999. Phase Distribution and Associated Phenomena on Oil–Water Flows In Horizontal Tubes Ph.D. thesis. Imperial College London.
Trallero, J.L., 1995. Oil–Water Flow Pattern in Horizontal Pipes Ph.D. thesis. The University of Tulsa.
Van Driest, E., 1956. On turbulent flow near a wall. J. Aeronaut. Sci. 23, 1007–1011.
Westerweel, J., Elsinga, G.E., Adrian, R.J., 2013. Particle image velocimetry for complex and turbulent flows. Annu. Rev. Fluid Mech. 45, 409–436.
Wright, S.F., Zadrazil, I., Markides, C.N., 2017. A review of solid–fluid selection options for optical-based measurements in single-phase liquid, two–phase liquid–liquid and multiphase solid–liquid flows. Exp. Fluids 58 (9), 108.
Yiantsis, S.G., Higgins, B.G., 1988. Linear stability of plane Poiseuille flow of two superposed fluids. Phys. Fluids 31, 3225–3238.
Yeh, Y., Cummins, H.Z., 1964. Localized fluid flow measurements with an HeNe laser spectrometer. Appl. Phys. Lett. 4, 176–178.
Yih, C.–S, 1967. Instability due to viscosity stratification. J. Fluid Mech. 27, 337–352.
Zadrazil, I., Markides, C.N., 2014. An experimental characterization of liquid films in downwards co–current gas–liquid annular flow by particle image and tracking velocimetry. Int. J. Multiph. Flow 67, 42–53.
Zadrazil, I., Matar, O.K., Markides, C.N., 2014. An experimental characterization of downwards gas–liquid annular flow by laser–induced fluorescence: Flow regimes and film statistics. Int. J. Multiph. Flow 60, 87–102.